Contents

1 Introduction

2 The ALEPH detector

The ALEPH detector is designed to study a wide range of phenomena produced in e^+e^- collisions, at first in the energy range of the Z, later up to 200 GeV. The results presented in this paper have been obtained around the Z resonance peak, where the events produced from Z decays can be complex, with particles distributed over 4π in solid angle. The detector thus was designed to have high three-dimensional granularity and hermetic coverage. A schematic diagram is shown in Fig. **??**. The apparatus and its performance have been described in detail elsewhere [1, 2]. An overview containing only essential information is presented here.

The origin of the ALEPH coordinate system is the nominal beam crossing point, the midpoint of the straight section between the two nearest LEP quadrupoles. The positive x axis points toward a vertical line through the LEP centre and is horizontal by definition. The positive z axis is along the nominal e^- direction. The y direction is orthogonal to x and z and points upwards.

2.1 Particle tracking

The tracking system involves three detectors: a silicon vertex detector, a conventional drift chamber and a large time projection chamber. These are contained within a 1.5 T magnetic field produced by a superconducting magnet coil.

The silicon vertex detector (VDET) [3], installed in 1991, is used for particle tracking close to the electron-positron interaction point and the vertex detector hits provide additional precision for tracks already reconstructed in the outer tracking. It consists of two concentric layers of double-sided silicon microstrip detectors positioned at average radii of 6.5 cm and 11.3 cm, covering respectively 85% and 69% of the solid angle.

The vertex detector is surrounded by a conventional multilayer axial-wire cylindrical drift chamber, the inner tracking chamber (ITC) [4], which is 200 cm long and measures the $r\phi$ positions of tracks at 8 radii between 16 and 26 cm. The average resolution in the $r\phi$ coordinate is 150 μm. The z coordinate is determined with a precision of a few cm by measuring the difference in arrival times of the signal at each end of the wires.

The time projection chamber (TPC) [5] is the main tracking chamber in the ALEPH detector. It provides 21 three-dimensional space coordinates and 338 samples of ionization energy loss (dE/dx) for fully contained tracks at radii between 30 and 180 cm. Requiring at least four points, tracks are reconstructed down to 15° in polar angle. An azimuthal coordinate resolution of 170 μm in $r\phi$ and a longitudinal resolution in z of 740 μm are obtained.

Using the combined information from the TPC, ITC and VDET, a transverse momentum resolution of $\sigma(1/p_T) = 0.6 \cdot 10^{-3}(\mathrm{GeV/c})^{-1}$ has been measured with 45 GeV muons from Z decays.

2.2 Calorimetry

The electromagnetic calorimeter (ECAL) is a lead/proportional wire chamber sampling device of 22 radiation lengths thickness, which surrounds the TPC. It is built in 36 modules, twelve in the barrel and twelve in each endcap, and covers 98% of the full solid angle. It is finely segmented in projective towers, each read out in three sections in depth ("storeys") of four, nine and nine radiation lengths. There are some 74,000 towers in all, each with an angular width of about $0.9^\circ \times 0.9^\circ$ providing detailed energy measurements in both azimuthal and polar angles. In addition, signals are available from the wire planes of each module allowing the measurement of the longitudinal shower development, provided other showers are not present in the same module. The relative energy resolution is $\sigma(E)/E = 0.18\sqrt{E} \oplus 0.009$ with E in GeV.

The superconducting coil provides a uniform 1.5 T magnetic field, which is returned in a large iron structure that is a fully instrumented hadron calorimeter (HCAL) and also serves as a muon filter. HCAL consists of 23 layers of streamer tubes 9×9 mm^2 in cross section separated by 5 cm thick iron slabs, giving a total of 7.2 interaction lengths. It is constructed from 36 modules, 24 in the barrel and 6 in each endcap, and is read out capacitatively in 4788 projective towers, each with a typical coverage of $3.7^\circ \times 3.7^\circ$. Digital signals from each of the tubes are also read out, providing a two dimensional projection of the energy deposition. Trigger signals are derived from the wires of the tubes. The relative energy resolution of the calorimeter is about $0.85/\sqrt{E(\mathrm{GeV})}$ for hadronic showers. The whole of ECAL is rotated in azimuth by about 2° with respect to HCAL to avoid overlapping of the small gaps ("cracks") between modules.

Outside the iron, are two double-layers of streamer tubes, the muon chambers, each providing two space coordinates for particles leaving the detector and hence improving the efficiency for muon identification. In 1990, only one such double-layer was present.

The luminosity detectors are described in Section 6.

3 The trigger system

The detector components used in the trigger for annihilation events are HCAL, ECAL, ITC, and TPC. All except the TPC cover nearly the same solid angle, which is a large fraction of 4π steradians. To monitor the e^+e^- collision rate, trigger signals from the luminosity calorimeters are used, as will be explained in Section 6. In order to establish the presence of particle signals in the various detector elements, the apparatus is divided in projective segments of solid angle, which closely follow the mechanical structure of the electromagnetic and hadronic calorimeters.

The trigger is organised into three levels. The level one provides a preliminary decision on whether there is a charged track using the ITC signals and/or particle energy from the calorimeters. The level two trigger seeks to verify a level one charged trigger by replacing the ITC tracking information with the more accurate TPC tracking information available 50 μs after the beam crossing. A level three software trigger is used to reject background such as beam-gas interactions and off-momentum particles hitting the vacuum chamber or collimator.

For Z decays three basic approaches are used at level one to derive the trigger signals.

- The total energy trigger is derived from the ECAL by summing separately the signals from the wire planes of the barrel modules and of the modules in each of the two endcaps. An energy above ∼6.6 GeV in the barrel, ∼3.8 GeV in either endcap, or ∼1.5 GeV in both endcaps is required by this trigger.
- The electromagnetic track trigger requires a track candidate in the ITC in coincidence with an energy deposit in the ECAL module to which the track is pointing. A track candidate is defined in the $r\phi$ plane by requiring hits in at least five out of the eight ITC layers. The associated ECAL wire energy must exceed ∼1 GeV.
- The muon track trigger is based on an ITC-HCAL coincidence, requiring a track candidate in the ITC in coincidence with four out of twelve double planes of HCAL tubes in the same azimuthal region.

In addition to these main triggers, two other subsidiary triggers are used to calculate the trigger efficiencies.

- An additional electromagnetic track trigger is defined based on a lower ECAL wires energy threshold (∼200 MeV) but with a more restrictive requirement on the ITC track, which must be defined in space, rather than in $r\phi$ only. This auxiliary trigger has a higher background acceptance than the main triggers. Therefore, depending on the data-taking period and circumstances it was either downscaled, or tightened, by requiring the presence of two track candidates in the drift-chamber, validated at level two.
- The back-to-back track trigger demands two track segments back-to-back in the ITC. The presence of such two charged particle trajectories must be confirmed by a level two decision.

3.1 Trigger efficiency

The trigger efficiency depends on the characteristics of the selected event sample and is determined in each case from the data using redundant trigger information.

The basic triggers for hadronic events are the total ECAL energy and muon track triggers. These triggers are entirely independent and separately cover more than 99.7% of the selected events. Their combined efficiency for hadronic Z decays exceeds 99.999%, with an uncertainty of less than 0.01%, which has been determined by comparing the rates for one or both of the triggers firing.

For the e^+e^- final states, the main trigger used are the total ECAL energy trigger and the charged electromagnetic track trigger. In the case of the the charged electromagnetic track trigger, the calculated efficiency is 0.99968 ± 0.00013 or better for all data compared with 0.99995 ± 0.00001 for the Monte Carlo. Requiring the total energy trigger to have fired results in no inefficiency seen in the Monte Carlo sample and efficiencies of 0.99999 ± 0.00001 or better for all the data samples considered.

Since all charged triggers rely on the ITC, the ECAL total energy trigger, which is totally independent on the ITC trigger signals, is also used to evaluate a potential bias to the trigger efficiency introduced by the ITC. This study makes use of Bhabha events, which in the ITC behave as $\mu^+\mu^-$ or $\tau^+\tau^-$, but always fire the ECAL total energy trigger. The resulting systematic uncertainty related to the ITC turns out to be of the order of 3×10^{-5}.

For the other leptonic final states the main triggers used are the electromagnetic and muon track triggers. Since these triggers are segmented in azimuth, the two leptons of a pair or their decay products trigger independently. Possible correlations due to insensitive regions between the calorimeter modules are found to have an impact of 0.03% on the efficiency. In fact, the bending of the magnetic field prevents back-to-back high momentum tracks both pointing to insensitive regions between modules. The single-lepton trigger efficiency is measured from the observed events and is used to calculate the overall efficiency for lepton pairs. Another cross-check of the trigger efficiency is obtained by comparing the rates of the main track triggers with auxiliary triggers. For this purpose the low threshold electromagnetic track and back-to-back track triggers are used for muons and the total energy and back-to-back track triggers for taus. Again no evidence of any inefficiency is observed.

.. No corrections applied to the efficiency? .. Any systematic effects?

4 LEP energy calibration

Good knowledge of the energy of the colliding particles at the interaction point is essential to a determination of the Z resonance parameters. A precise determination of the mass and width of the Z was achieved by changing the beam energies from fill to fill, where one fill typically lasted about 10 h and delivered an integrated luminosity of several hundred pb^{-1}. In 1993 and 1995, data were recorded close to three different energies called 'energy points', near the maximum of the resonance (called 'peak') and about two GeV below and above ('peak−2' and 'peak+2'); data taking in 1992 and 1994 was exclusively at the peak point; in 1990 and 1991 data were collected at several different energy points with centre-of-mass energies in the range $|\sqrt{s} - M_{\mathrm{Z}}|<3$ GeV.

The uncertainty in the absolute energy scale, i.e., uncertainties correlated between the energy points, directly affect the mass, whereas the width is only affected by the error on the difference in energy between energy points. The errors induced on the mass and width of the Z depend mainly on the high statistics peak±2 points in 1993 and 1995 and are approximately given by

$$\begin{array}{rcl} \Delta M_{\mathrm{Z}} & \approx & 0.5\ \Delta(E_{+2}+E_{-2}) \\ \Delta\Gamma_{\mathrm{Z}} & \approx & \frac{\Gamma_{\mathrm{Z}}}{E_{+2}-E_{-2}}\Delta(E_{+2}-E_{-2}) \\ & = & 0.71\ \Delta(E_{+2}-E_{-2})\ , \end{array} \tag{1}$$

where E_{+2} and E_{-2} are the luminosity-weighted average centre-of-mass energies at peak+2 and peak−2. The effects of the beam energy calibration on the pole cross section and on the forward-backward asymmetries are smaller (see discussion in Section 11).

An accurate determination of the average energy of the beams in LEP [6] is based on the technique of resonant depolarisation [7] characterised by a very high precision (± 0.2 MeV) at the time of the measurement. However, these measurements were practically possible outside normal data taking only, typically at the end of fills. Therefore, other techniques had to be used to trace back the very precise energy determination to earlier times in a fill and to those fills where no calibrations by resonant depolarisation could be made. The integrated luminosity taken during calibrated fills at the peak±2 points corresponded to 40% and 70% in 1993 and 1995, respectively. In addition, six fills could be calibrated before physics data taking started. These measurements were particularly useful for the understanding of changes in beam energy during fills.

The extrapolation of these well-known values of the beam energy at a particular time to the full set of data required a modelling of the dependence of the magnetic field of the bending dipole magnets on current and temperature as well as a precise understanding of changes in energy caused by geometrical deformations of the LEP ring. The level of agreement of these models with reality could be checked by comparison with the precise depolarisation measurements and with direct measurements of the magnetic dipole fields by nuclear magnetic resonance probes.

The energy at the interaction point is not equal to the mean beam energy discussed so far. The acceleration of the particles in the radio frequency cavities at the interaction points 2 and 6 (the position of the ALEPH detector corresponds to point 4) and dispersion effects (i.e., an energy ordering of particles in a bunch) can lead to substantial corrections on the mean beam energy. In ALEPH, such corrections were small. The RF correction was negligible in 1993 and only ∼1.0 MeV in 1995. The dispersion correction was shown to be negligible in 1993 and ∼0.5 MeV in 1995.

The mean beam energy was determined every 15 minutes and was used as an input to the data analysis. The errors on these values were assumed to be the same at all times and are summarised in Table 1.

Although the errors at different interaction points are slightly different due to different RF configuration and varying beam dispersion, only one set of errors is given; strictly speaking this is only valid after combining the results of the four LEP experiments. **!!! no special ALEPH matrix available yet; if it comes,this piece of text will go !!!**

The energy of a given particle in a bunch oscillates around the mean energy with a frequency which is given by the synchrotron tune of the accelerator multiplied with the revolution frequency. Therefore, the colliding particles are typically not exactly at the mean energy de-

	‘93 peak−2	‘93 peak	‘93 peak+2	‘94 peak	‘95 peak−2	‘95 peak	‘95 peak+2
‘93 peak−2	3.46^2	2.80^2	2.63^2	2.29^2	1.30^2	1.20^2	1.22^2
‘93 peak		6.71^2	2.68^2	2.42^2	1.15^2	1.21^2	1.17^2
‘93 peak+2			2.99^2	2.21^2	1.24^2	1.27^2	1.34^2
‘94 peak				3.70^2	1.24^2	1.31^2	1.25^2
‘95 peak−2					1.82^2	1.27^2	1.26^2
‘95 peak						5.41^2	1.37^2
‘95 peak+2							1.72^2

Table 1: The covariance matrix of the uncertainties on the centre-of-mass energies (in MeV^2) for the scan points in 1992-1995.

scribed above. The energy spread δE is readily calculable from machine parameters and can be checked using the longitudinal size of the bunches, measured from the longitudinal size of the luminous region at the ALEPH interaction point. The values of the centre-of-mass energy spread determined for ALEPH are shown in Table 2. This energy spread has to be taken into account when correcting the cross section measured at one energy point to a sharp value in centre-of-mass energy.

	energy spread [MeV]		
	peak−2	peak	peak+2
1990		46.	
1991		46.	
1992		51.	
1993	54.6	55.4	55.6
1994		54.9	
1995	55.7	56.2	56.6

Table 2: Centre-of-mass energy spread. The uncertainties on the energy spread are ±5 MeV in 1992 and before, ±1.1 MeV in 1993 and 1994 and slightly larger, 1.3 MeV, in 1995 due to dispersion at the interaction points. Note that the additional energy spread of about 10 MeV from differences in mean beam energy of data taken at an energy point has to be added in quadrature to the numbers quoted above.

5 Data and Monte Carlo samples

The results presented here are based on the entire LEP1 dataset, that is the data collected by ALEPH between 1990 and 1995. The efficiency of the ALEPH detector with respect to the integrated luminosities delivered by LEP is 83.4% averaged over all years, reaching 90% in 1995. The main causes for the inefficiency are operational (mainly due to the detector not yet being at full voltage when stable beam conditions are reached at the beginning of fill or to high-voltage trips (35%)), or are associated to the detector data acquisition dead time (27%) or to data acquisition or hardware faults (38%). In addition, approximately $x\%$ of the data are rejected off-line due to occasional malfunctioning of the detector components which are relevant for the analyses presented here. A final check is performed off-line on an event-by-event basis to reject those events affected by high-voltage trips of the major detector components mainly initiated by high machine background conditions.

5.1 The data sample

The data are divided in 27 different energy points according to centre-of-mass energy and year. Throughout the rest of this paper, the various parts of the LEP1 dataset will be referred to using the conventional names specified in Table 3. In 1992, due to the upgrade of the luminosity calorimeter, two different luminosity setups were present for which the data were analysed separately, the 1992 'LCAL' and 'SiCAL' periods. In 1993 and 1995, the data taking periods were divided into two parts. In the 'scan' period, data were collected at three energy points in turn, with frequent LEP energy calibration measurements distributed throughout the period, as discussed in Section 4. Before the start of the scan, data were collected at the peak energy. Such periods for which the LEP energy uncertainties are significantly larger than those of the scan points are referred as 'prescan' data. No SiCAL luminosity is available for the periods 'peak_no_SiCAL' of 1994 and 'prescan' of 1995 due to bad LEP background conditions in 1994 and variable bunch train configuration in 1995.

5.2 Monte Carlo samples

To design the selection algorithms, several large Monte Carlo event samples were generated and processed through the complete detector simulation and event reconstruction. The detector simulation takes into account variations in the response of the apparatus from one year to the next. Details on the various Monte Carlo data sets used for the analysis can be found in Appendix B.

The event generator KORALZ 4.0 [8] was used to produce $\mu^+\mu^-$ and $\tau^+\tau^-$ events. This program includes initial and final state bremsstrahlung corrections up to order $O(\alpha^2)$ with exclusive exponentiation, and $O(\alpha)$ electroweak corrections. However QED initial-final bremsstrahlung interference in the presence of multiple QED hard bremsstrahlung is not included. Approximately 900 K $\mu^+\mu^-$ and 1.1 million $\tau^+\tau^-$ were generated at the different nominal centre-of-mass energies (peak, peak$\pm$1, peak$\pm$2, peak$\pm$3).

Wide-angle Bhabha events were produced using program UNIBAB [9]. UNIBAB is an event generator which contains leading log contributions to the electromagnetic radiative corrections to all orders in a Monte Carlo branching algorithm, with soft photon exponentiation as well as contributions from multiple emission of hard collinear photons. Since the radiated photons are generated explicitly, the full kinematic information on the multi-photon emission is available. UNIBAB has no provision for the interference between initial and final state radiation. Approximately 550K e^+e^- events were generated at the different centre-of-mass

year	'Name'	$\sqrt{s}$ [GeV]	integrated Luminosity recorded by ALEPH [nb^{-1}]
1990	peak	91.214	3624.0
	peak+1	92.206	554.6
	peak+2	93.208	597.2
	peak+3	94.201	641.8
	peak−1	90.216	447.2
	peak−2	89.216	520.1
	peak−3	88.222	482.0
1991	prescan	91.226	7546.4
	peak		
	peak+1	91.952	693.2
	peak+2	92.952	677.3
	peak+3	93.701	796.6
	peak−1	90.212	753.2
	peak−2	89.456	796.8
	peak−3	88.464	668.4
1992	LCAL	91.276	12297.6
	SiCAL	91.270	8749.0
1993	prescan	91.285	5311.1
	peak	91.184	9134.6
	peak+2	93.012	8689.9
	peak−2	89.430	8069.2
1994	peak	91.194	42692.3
	peak_no_SiCAL	91.215	—
1995	prescan	91.279	—
	peak	91.279	4872.1
	peak+2	92.969	9372.6
	peak−2	89.439	8121.3

Table 3: Integrated luminosities recorded by ALEPH at the various energy points and luminosity-weighted average energies for the years 1990 to 1995.

energies in a restricted polar angle region (as specified in Section 9.3) to avoid divergencies due to the t-channel exchange.

Hadronic events were produced with program HVFL, which incorporates several components. The initial quark-antiquark pair and initial state photon radiation are generated with program DYMU [10]. These are then passed to the Lund Parton Shower Model [11] (program JETSET version 7.3), in which the decay properties of heavy flavour hadrons have been significantly extended. Approximately ???? events were generated at the peak. In addition about one million events were generated off-peak without, however, being processed through the detector simulation program. The off-peak efficiencies were therefore computed from the sample of fully reconstructed events at the peak point, to which a correction determined at the generator level was applied.

Four-fermion processes of the type $\mathrm{e^+e^-} \to \ell^+\ell^-\mathrm{f\bar{f}}$ where l is a lepton and f any fermion were simulated using the four-fermion generator FERMISV [**?**]. Details on the generation and the impact of such processes on the lepton cross section measurements are discussed extensively in Section **??**.

Initial state radiation (ISR) lowers the invariant mass of the final state particles including final state radiation, $\sqrt{s'}$. Therefore the $\mathrm{e^+e^-} \to \mathrm{f\bar{f}}$ reaction occurs as if a scan of the non-radiative region were performed from $s' = 4m_{\mathrm{f}}^2$ to $s' = s$. In the generation of both muon- and tau-pairs, the minimum invariant mass of the $\mathrm{f\bar{f}}$ system, was set to twice the tau mass, while for hadrons it was set to $0.1\sqrt{s}$. These values applied to the Monte Carlo event generation to determine detector acceptances must coincide with the integration bounds for the initial state radiation used in the fitting function described in Section [**?**].

The small-angle Bhabha Monte Carlo event samples used for the luminosity determination are described in Section 6.

6 The Luminosity determination

6.1 The Luminosity measurement at LEP I

Bhabha scattering $\mathrm{e^+e^-} \to \mathrm{e^+e^-}$ is used as the reference reaction in $\mathrm{e^+e^-}$ experiments. The rate of such events detected in specially designed monitors is used to measure the absolute luminosity of the colliding beams, found by dividing the number of monitored events by the Bhabha cross section integrated over the acceptance. The cross sections for the processes studied in a colliding-beam detector are then determined with respect to the absolute luminosity given by the reference reaction. At LEP energies this technique is used in precision measurements of the Z resonance cross sections, which are essential for the determination of the number of light neutrino species, as well as the Z parameters. The effect of electroweak process $\mathrm{Z} \to \mathrm{e^+e^-}$ on the reference cross section can be limited by restricting the acceptance to low angles where the Bhabha rates are dominated by small values of four-momentum transfer and therefore largely described by quantum electrodynamics (QED). The large cross section at low angles gives a further advantage of reducing the statistical uncertainty of the reference measurement.

Two generations of Luminosity detectors were used in ALEPH during the LEP I lifetime. The first one, consisting of a lead/proportional wire sampling calorimeter (LCAL) with a track detector in front (SATR), was used from 1889 to September 1992. The second one, a silicon-tungsten sampling electromagnetic calorimeter (SiCAL), was used from September 1992 till the end of LEP I running in October 1995.

6.2 General considerations

1. Mechanical design constraints: At LEP the size of the luminous region is small ($\sigma_x \simeq$ 0.14 mm, $\sigma_y \simeq 0.003$ mm, and $\sigma_z \simeq 7$ mm) with respect to the scale of the distance

to the detectors ($\simeq$ 2500 mm), thus once the background and detection efficiencies are under control, the limiting source of systematic error in the measurement is given by the error in the acceptance at the lower θ bound. At small angles the lowest order QED Bhabha cross section is simply:

$$\frac{d\sigma}{d\Omega} = \frac{16\,(\hbar c\alpha)^2}{s}\left(\frac{1}{\theta^4}\right) \tag{2}$$

which integrated over the acceptance gives:

$$\sigma^{\mathrm{acc}} = \frac{1040 \text{ nb GeV}^2}{s}\left(\frac{1}{\theta^2_{\mathrm{min}}} - \frac{1}{\theta^2_{\mathrm{max}}}\right) \;, \tag{3}$$

where the polar angular bounds can be defined as radial limits at a defined distance along the z axis from the interaction point : $\theta_{\mathrm{min}} \rightarrow R_{\mathrm{min}}$ and $\theta_{\mathrm{max}} \rightarrow R_{\mathrm{max}}$.

The importance of the knowledge of the absolute position of the radial acceptance limit can be seen by considering the change in the measured cross section due to a displacement of the inner radial acceptance bound:

$$\frac{\delta\sigma^{\mathrm{acc}}}{\sigma^{\mathrm{acc}}} = \frac{2\delta R}{R_{\mathrm{min}}}\left(1 + \frac{R^2_{\mathrm{min}}}{R^2_{\mathrm{max}} - R^2_{\mathrm{min}}}\right), \tag{4}$$

which implies that a given desired overall precision requires control of the absolute value of the radial bound to the corresponding mechanical precision.

2. Trigger design: Triggers used in the luminosity determination have to be highly efficient for Bhabha scattering events and redundant to allow independent checks of the trigger efficiency. Furthermore, as the principal source of background to Bhabha scattering at LEP is the accidental coincidence of off-momentum beam particles, a dedicated trigger is setup to allow a precise determination of this contamination.

   Three triggers, based on the total energy deposition in the calorimeters, have been used throughout the LEP I running.

   - A luminosity trigger, which requires a large energy deposit in one end-cap calorimeter together with a less restrictive energy requirement in the other. This trigger is called $(A_{\mathrm{low}} \cdot B_{\mathrm{high}}) + (A_{\mathrm{high}} \cdot B_{\mathrm{low}})$. Typically, the low and high thresholds were 10(12) GeV and 22(24) GeV, respectively, for LCAL(SiCAL).
   - A very-high threshold single-arm trigger, requiring at least 35(39) GeV energy deposit on either side, allows the efficiency determination of the luminosity trigger. It is prescaled to be a small contributor to the overall ALEPH trigger rate.
   - A very-low threshold prescaled single-arm trigger, requiring at least 15(9) GeV energy deposits on either side, is used to estimate the beam related background rate and shape.

3. Event selection:

   Despite the different characteristics of the two successive luminometers which translate in improved experimental systematic errors, a consistent event selection has been applied to LCAL and SiCAL luminosity triggers.

- Energy cuts: Event selection is based on energy clusters reconstructed in each side calorimeter. As Bhabha scattering events generally have radiated photons which may or may not be distinguishable from the "primary" energy cluster, no upper limit on the number of clusters found is imposed. The highest energy one is chosen on each side to define the barycentre position. A typical picture of the energy correlation between both sides is given in Figure 1. The energy deposited on each side is required to be larger than 44% of the beam energy while the sum of the two energies must be larger than 60% of the centre of mass energy. This set of energy cuts has been used up to 1993 included. The cut on the energy sum was increased in 1994 and 1995 due to higher contamination of beam-related background. Figure 2 shows the evolution of the total energy cut with year of data taking.

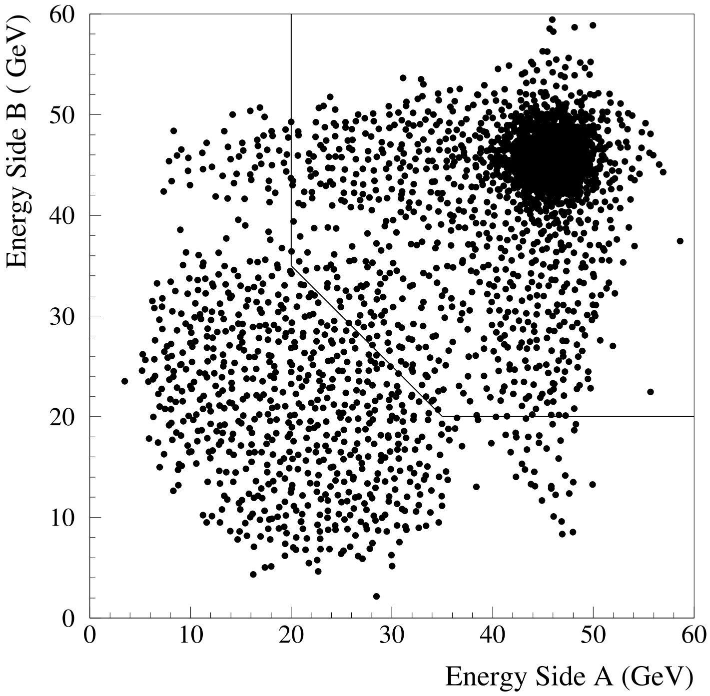

Figure 1: SiCAL largest reconstructed cluster energy on side-A versus largest reconstructed cluster energy on side-B (GeV).

- Radial fiducial cuts: Radial cuts define the Bhabha acceptance.The radial fiducial selection is based upon radial energy sharing between adjacent pads at the fiducial boundary, summed over two layers in depth at $6X_0$ and $8X_0$. The radial energy asymmetry A_r is defined by:

$$A_r = \frac{E_{in} - E_{out}}{E_{in} + E_{out}}, \tag{5}$$

where E_{in} is the energy inside a radial pad-width within the fiducial region and E_{out} is the energy in the adjacent pad-width outside the region. A "tight" fiducial

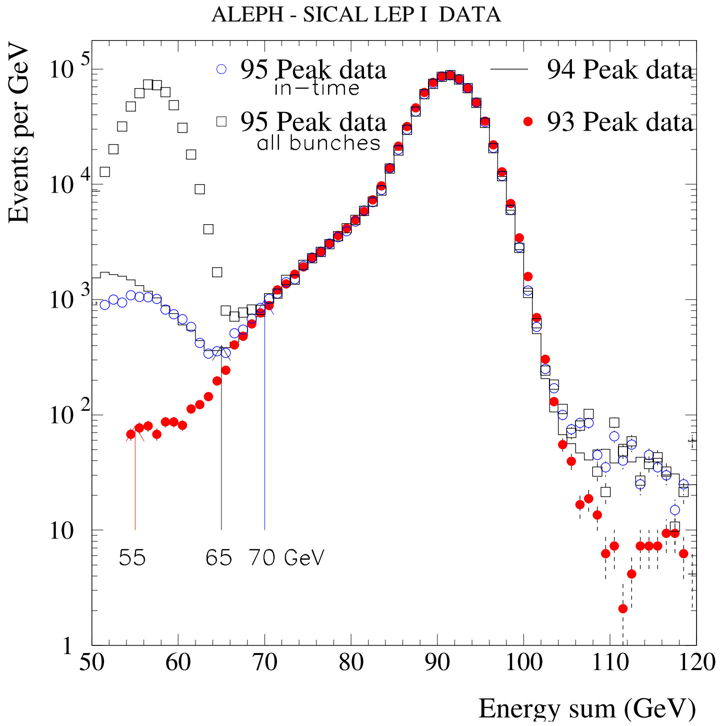

Figure 2: SiCAL energy sum distribution for clusters satisfying radial and azimuthal requirements. The different levels of beam-related background and the bunch train operation mode in 1995 justify the evolution of the cut on the energy sum as indicated by the arrows.

selection on one side and a "loose" fiducial selection on the opposite side, alternated event by event, reduce the sensitivity of the selection to beam offsets. The tight side is sufficiently constrained to ensure full containment of showers from Bhabha events whereas the loose side permits clusters to lie within a larger area.

- Acoplanarity cut: Bhabha events are essentially coplanar, except for radiated photons. An acoplanarity cut based upon the two clusters azimuthal difference, $150° \leq \Delta\phi \leq 210°$, is used to remove the remaining off-momentum beam background without severely cutting away the radiative Bhabha events. Figure 3 shows the typical $\Delta\phi$ distribution in various background conditions.

6.3 LCAL Luminosity measurement

A detailed discussion of the LCAL Luminosity measurement was already published in [12]. The LCAL lead-proportional wire chamber calorimeter covers the polar angle region from 46 to 122 mrad. Up to 1991 it has been used in conjunction with a small angle tracker (SATR) which was removed in 1992 to permit the installation of the SiCAL. The evaluation of the systematic error for each year proceeded in the same way as described in [12]. To check the

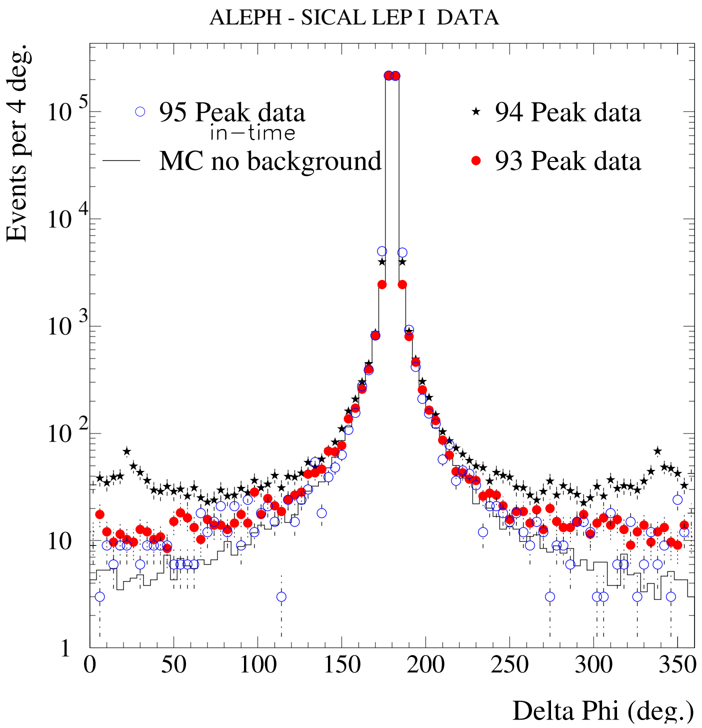

Figure 3: Distribution of the ϕ-difference $\Delta\phi$ between the "tight-side" and "loose-side" clusters. Data from different years are plotted as points(stars) and the Monte Carlo (without background) is shown as a line. Depending on the energy sum cut applied, different level of background were achieved.

accuracy of the understanding of the acceptance, the results using two different fiducial-side selections, differing by one more padrow inside the detector on the tight side, were compared. The difference using all LCAL data from 1989 to 1992 is compatible with a systematic error of 0.21%, whose determination with this method has fluctuated statistically from year to year. The total LCAL experimental systematic errors for all years are estimated to be: 0.49% (1989–1990), 0.38% (1991) and 0.37% (1992 LCAL period).

6.4 SiCAL Luminosity measurement

The SiCAL is a silicon-tungsten sampling electromagnetic calorimeter, 23 radiation lengths (X_0) in depth. It consists of two homogeneous cylindrical detectors surrounding the beam pipe at roughly ± 250 cm from the interaction point. The calorimeters cover the polar angular range from 24 to 58 mrad. Twelve layers of tungsten alternate with layers of silicon pad detectors. Each layer is segmented into 32 sectors in azimuth, each with 16 radial pad rows 5.225 mm wide. A total of 12288 pads are readout individually, allowing a full reconstruction of the transverse and longitudinal shower development. The internal alignment of the silicon detector elements and the measurement of the separation between half modules with a light-emitting diode optical system ensure a mechanical precision of the radial fiducial boundary of 9μm.

The analysis of the SiCAL luminosity is largely based upon the previous LCAL analysis, simplified by the homogeneity of the new detector. The tight side is sufficiently constrained to ensure full containment of showers from Bhabha events (radial pad rows 4 to 12, inclusively), whereas the loose side permits clusters to lie within pad rows 2 to 15, inclusively. A looser tight cut (radial pad rows 3 to 12, inclusively) was used as well to control the acceptance. The total energy sum requirement had to be increased with successive years as the contribution from off-momentum electrons became larger. This allowed to keep the systematic error from that source at a very low level while the one due to the energy cut was increased. However, this compromise ended in a total experimental systematic error well controlled below the 0.1%.

6.5 Systematic errors and correlations

Trigger efficiency and background estimation are very well controlled using the data for both luminosity calorimeters. The most critical item contributing to the systematic error is the absolute radial fiducial boundary knowledge. It depends upon the mechanical precision but also upon the relative beam and module alignments which have a sizeable spread. Precise measurements of the Sical support plates under operating temperature allowed a precise determination of the thermal distortion and led to a total "effective" radial uncertainty of 9μm, helping reducing that particular contribution. The summary of the absolute luminosity systematic errors is presented in Table 4 for SICAL luminosity measurements from 1992 to 1995. Systematic errors are expressed as relative errors. Typical correlated systematic errors are given in Table 5 for any two years between 1992 and 1995. The total uncorrelated 1995 point to point error is 0.056% (summarised in Table 6). The increase from 0.038% in 1993 is due to the much higher energy sum cut applied.

Table 7 gives the correlation coefficients ($\sigma^2_{\mathrm{corr}}/(\sigma_{\mathrm{year1}}\sigma_{\mathrm{year2}})$) among luminosity errors for all the years.

6.6 Theoretical uncertainty

Two successive versions of a Bhabha generator BHLUMI were used in the Luminosity analyses. BHLUMI version 2.01 [14] was used for the analysis of the data up to 1992 with a 0.16% theoretical uncertainty in a Sical-like acceptance. BHLUMI version 4.04 [15] was used in later years, with a 0.11% error in the same conditions. Version 4.04 of BHLUMI allows an improved calculation of the contribution of the Z resonance to the small angle Bhabha scattering process and includes second-order terms in the leading-logarithmic approximation for the multi-photon YFS exponentiation. The Z contribution implementation was cross-checked against the BABAMC calculations performed for the analysis of the four energy points of the 1993 scan [16] and found to be in good agreement. Table 8 summarises the total theoretical uncertainty for Lcal and Sical acceptances at LEP I.

Source of uncertainty	1992 SICAL Period	1993 EW Selection	1994 EW Selection	1995 EW Selection
Trigger efficiency	0.0010%	0.0002%	0.0006%	0.003%
Background estimation:				
- Off momentum e^+ or e^-	0.018%	0.003%	0.0007%	0.0009%
- Physics sources	0.010%	0.010%	0.010%	0.010%
Reconstruction efficiency	0.001%	0.001%	0.001%	0.001%
Event migration from overlays	$< 0.005\%$	nil	0.008%	0.003%
Absolute radial fiducial boundary:				
- Mechanical precision	0.058%	0.029%	0.029%	0.029%
- Beam and module alignments	0.035%	0.030%	0.031%	0.030%
- z position of modules	0.035%	0.035%	0.035%	0.035%
- Asymmetry precision	0.044%	0.025%	0.030%	0.030%
- Simulation precision	0.023%	0.016%	0.016%	0.016%
Energy cuts	0.015%	0.004%	0.015%	0.038%
Acoplanarity cut	0.005%	0.005%	0.005%	0.005%
R-width cut related sources:				
- following wagon contamination				0.0006%
- preceding wagon contamination				0.001%
SUBTOTAL	0.095%	0.063%	0.069%	0.076%
Simulation statistics	0.120%	0.024%	0.024%	0.026%
TOTAL experimental error	0.153%	0.067%	0.073%	0.080%
Theoretical error	0.160%	0.110% †	0.110% †	0.110% †
TOTAL LUMI error	0.221%	0.129%	0.132%	0.136%

Table 4: Summary of absolute luminosity measurement systematics. The theoretical error marked with † was improved using the newer BHLUMI version 4.04, while version 2.01 was used for the 1992 cross sections calculations.

7 Common analysis tools

An important feature of the ALEPH detector is its particle identification capability arising from the high segmentation of the calorimeters. The analyses described here rely mainly on topological selection criteria. However particle identification is used to separate the various

Source of uncertainty	Correlated systematics 199x-199y
Trigger efficiency	nil
Background estimation:	
- Off momentum e^+ or e^-	0.0007% to 0.003%
- Physics sources	0.010%
Reconstruction efficiency	0.001%
Absolute radial fiducial boundary:	
- Mechanical precision	0.027%
- Beam and module alignments	0.015%
- z position of modules	nil
- Asymmetry precision	0.025%
- Simulation precision	0.016%
Energy cuts	0.004%
Acoplanarity cut	0.005%
R-width cut	nil
SUBTOTAL	0.044%
Simulation statistics	nil
TOTAL correlated experimental error	0.044%
Revised Theoretical error †	0.11%
TOTAL Correlated LUMI error	0.118%

Table 5: Summary of absolute luminosity measurement correlated systematic uncertainties between 1995 and previous years. The theoretical error for 1993,1994 and 1995 (†) was revised using the new BHLUMI version 4.04.

leptonic channel, and the principal features of the algorithms used are briefly described here.

7.1 Muon identification

Muons are identified by making use of the tracking capabilities of the hadron calorimeter, together with the muon chamber information. The HCAL digital readout is used to check whether particles penetrate through the whole depth of the calorimeter. Tracks are extrapo-

Source of point to point uncertainty	1993 EW Selection	1995 EW Selection
Beam related systematics	0.021%	0.021%
Energy resolution	0.006%	0.041%
Shower shape and asymmetry cut	0.008%	0.008%
Use of KINGAL cross section	0.006%	0.005%
SUBTOTAL point to point	0.024%	0.047%
Simulation statistics	0.024%	0.026%
TOTAL experimental point to point error	0.034%	0.054%
Theoretical point to point error	0.017%	0.017%
TOTAL uncorrelated error	0.038%	0.056%

Table 6: Summary of SICAL final 1993 and 1995 point to point luminosity measurement systematics.

SICAL Year	1992	1993	1994	1995
1992	1.	0.488	0.477	0.463
1993		1.	0.818	0.794
1994			1.	0.776
1995				1.

Table 7: Summary of correlation coefficients between 1992, 1993, 1994 and 1995 luminosity errors. The values for the 1993 and 1994 correlations have been revised according to the new theoretical error.

lated through the calorimeter material taking into account a detailed magnetic field map and estimated energy losses. A 'road' is opened around the extrapolated track, with a width of three times the estimated extrapolation uncertainty due to multiple scattering. A calorimeter plane is said to be expected to fire if the extrapolated track intersects it within an active region, and the plane is said to have fired if a digital hit lies within the multiple scattering road.

BHLUMI version	2.01	2.01	4.04
	Lcal	Sical	Sical
(1) missing photonic $\mathcal{O}(\alpha^2 L)$	0.15 %	0.15 %	0.10 %
(2) missing photonic $\mathcal{O}(\alpha^3 L^3)$	0.03 %	0.008%	0.015%
(3) Vacuum polarisation	0.008%	0.05 %	0.04 %
(4) Light pairs	0.08 %	0.04 %	0.03 %
(5) Z-exchange	0.12 %	0.03 %	0.015%
TOTAL (quadratic sum)	0.21 %	0.16 %	0.11 %

Table 8: Summary of the total (physical + technical) theoretical uncertainty for a calorimetric detector and an angular range within $3^o - 6^o$ (Lcal) and $1^o - 3^o$ at LEP I (Sical).

A track is defined to have hits in the muon chambers if at least one of the two double-layers yields a space point whose distance from the extrapolated track is less than four times the estimated standard deviation from multiple scattering.Typically a track is considered to be a muon if more than nine planes fired in total, more than four of the last ten planes fired and the track extrapolates to within 4 σ of a hit in the muon chambers. The muon identification implies an implicit momentum cut. In fact the muon chambers hit association is performed only for tracks with momenta larger than 2.2 GeV/c, while the HCAL information are available for tracks with momenta larger than 1.5 GeV/c.

7.2 Electron and photon identification

Electron identification is performed using two independent and complementary measurements, the energy deposition in ECAL and the dE/dx measurement from the TPC. The former is most effective above 5 GeV, the latter is better at low energy.

Identification in ECAL is based on two estimators which measure the degree to which an energy deposit near a track extrapolated from the TPC conforms to that expected for an electron. Both compactness of electromagnetic energy deposition around the original particle direction and the longitudinal shape of the shower are exploited. Using these variables alone the electron efficiency is about 98% for isolated particles with energy above 2 GeV outside cracks and the overlap regions. The pion misedintification rate is less than 1%. A similar procedure is used for photon identification with the requirement that no charged track points to the electromagnetic cluster.

In conjunction with these estimators, a third one can be used, based on the dE/dx measurement for a track in the TPC compared to the mean value expected for electrons.

7.3 Energy flow reconstruction

An energy flow reconstruction algorithm was developed which makes use of the track momenta and of the identification capabilities of the detector. Briefly, charged particle tracks are extrapolated to the calorimeters and groups of topologically connected tracks and clusters, called 'calorimeter objects', are formed. Charged particle tracks identified as electrons, muons or charged hadrons and neutral electromagnetic energy objects identified as photons are removed from the 'calorimeter objects', leading to residual neutral hadrons. As a result, the analysis programs are supplied with a list of 'energy flow objects' (electrons, muons, photons, charged or neutral hadrons), characterised by their energies and momenta,

7.4 Definitions and notations

The event selections for most of the analyses are based on tracks of charged particles. Tracks are selected that have at least four measured space coordinates in the TPC. In addition the distance of closest approach of the tracks to the origin must be less than ± 10 cm along the beam direction, z_0, and less than 5 cm transverse to it, d_0. These tracks will be hereafter referred as 'good'.

Event hemispheres are defined by dividing the events into two using the plane perpendicular to the thrust axis. If at least one good track is found in each hemisphere, the acollinearity η is defined as $180°$ minus the angle between the two highest momentum tracks. For tau events, the acollinearity is calculated from the vector sum of all energy flow objects in each hemisphere.

In the lepton-pair selections the scattering angle, θ^*, between the incoming e^- and the outgoing fermion is defined as

$$\cos\theta^* = \frac{\cos\left[\frac{1}{2}\left(\theta_{\mathrm{l}^-} - \theta_{\mathrm{l}^+} + \pi\right)\right]}{\cos\left[\frac{1}{2}\left(\theta_{\mathrm{l}^-} + \theta_{\mathrm{l}^+} - \pi\right)\right]}, \tag{6}$$

where θ_{l^-} and θ_{l^+} are the polar angles of the two highest momentum lepton and antilepton, respectively. For taus, the lepton direction is defined as the vector sum of all objects in the hemisphere. The variable $\cos\theta^*$ preserves the angular distribution in the $\mathrm{e}^+\mathrm{e}^-$ centre-of-mass when hard collinear radiation takes place from the initial state.

8 Measurement of the hadronic cross section

Events from hadronic Z decays are selected in two independent ways, leading to a reduced systematic error for the average of the two methods. One selection is based on charged tracks only, the other on calorimetric energy. Both methods have an efficiency close to unity, and the two data samples used in the analysis overlap to the extent of 95%. *Check this..*

8.0.1 The selection based on charged tracks

The selection based on charged tracks, using few cuts, requires at least five good charged particle tracks in the TPC. These tracks are required to have a polar angle ensuring that at least six pad rows are crossed, i.e., $\cos\theta < 0.95$ and their distance of closest approach to the origin in the transverse plane must be less than 2 cm. In addition the sum of the energies of the tracks (assuming the pion mass) is required to be larger than 10% of the centre-of-mass energy. The effect of these cuts is illustrated in Figure 4 where the most significant background reactions are well isolated. Lepton pairs are removed by the cut on track multiplicity (N_{TPC}) whereas 2-photon events are rejected by the total energy requirement (E_{TPC}).

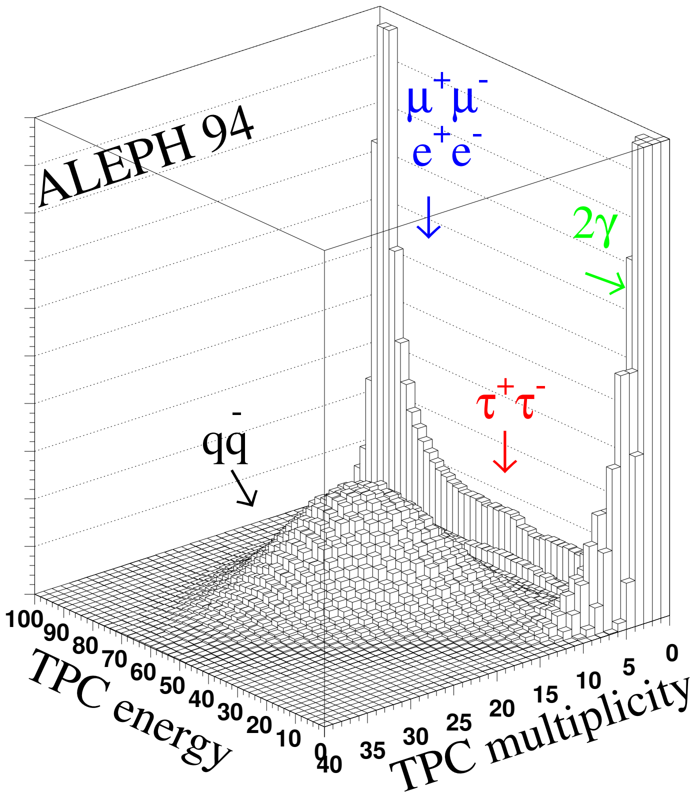

Figure 4: Events selected with the hadronic triggers, as a function of their charged multiplicity and energy.

The charged energy and multiplicity requirements are highly correlated: more than 85% of the events are in fact rejected by both cuts. The selection results in an overall efficiency of 97.477% at the peak point, where the loss of efficiency comes essentially from low-angle events. As pointed out in Section 5.2, the off-peak efficiencies were calculated from the sample of fully reconstructed Monte Carlo events generated at the peak point, to which a correction was applied, determined from Monte Carlo samples produced off-peak at the kinematic level only. The resulting efficiencies shown in Figure 5 reveal a slight but appreciable dependence on centre-of-mass energy. This variation stays within 0.1% of the efficiency at the peak and can be explained by ISR photons reducing the effective centre-of-mass energy available, particularly above the peak. Since the selection efficiency decreases for lower values of s'/s, this reflects into lower efficiencies off-peak.

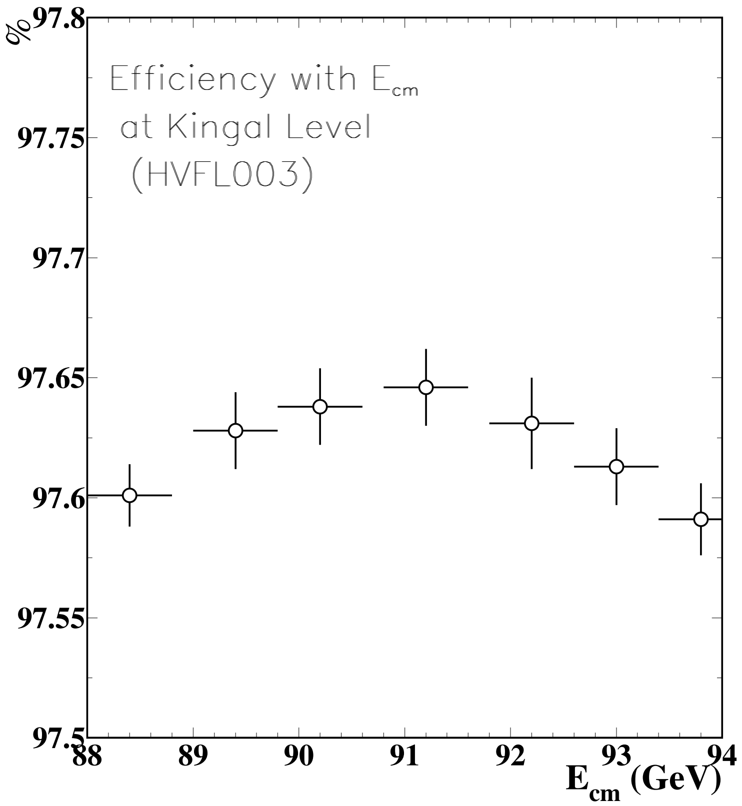

Figure 5: Efficiency as a function of centre-of-mass energy.

The background to the hadronic selection originating from dilepton-pairs is estimated from Monte Carlo. The contamination from both electrons and muons is found to be negligible, whereas the background arising from $\tau^+\tau^-$ events is computed to be 0.32%, as shown in Table 9, and its uncertainty gives a 0.03% contribution to the systematic error. Background from beam-gas interactions is estimated from the number of events passing all selection cuts except for the requirement of the vertex position along the beam. It is found to be negligible.

Contrary to the leptonic backgrounds which affect the measurement of the absolute cross section, the background from two-photon processes, $\mathrm{e^+e^-} \rightarrow \mathrm{e^+e^-}+$ hadrons, enters as one of the main sources of uncertainty to the Z width. As shown in Fig. 4, below the cut $0.10\sqrt{s}$ this background is dominant. The contamination in the accepted sample is estimated from the data by exploiting the different centre-of-mass energy dependence of resonant and non-resonant contributions.

Let $\sigma_{\mathrm{i}}(\sqrt{s})$ denote the cross section measured at centre-of-mass energy $\sqrt{s}$ for events with charged energy $E^{\mathrm{i}}_{\mathrm{TPC}}$ comprised in an interval i of 1 GeV width. This cross section

	Hadronic selection	
	Charged track	Calorimeter
Efficiency	97.477%	99.xx%
Background:		
$\tau^+\tau^-$	0.32%	0.xx%
$\gamma\gamma$ (pb)	7x±xx	7x±xx
e^+e^- (pb)	negl.	
Source of systematics		
detector response	0.02%	0.0x%
modelling	0.063%	negl.
MC statistics	0.02%	0.0x%
background:		
$\tau^+\tau^-$	0.03%	0.0x%
$\gamma\gamma$	0.04%	0.0x%
e^+e^-	negl	
Total systematics	0.087%	0.121%
combined	0.073%	

Table 9: Efficiency, background and systematic errors for hadronic selections at the peak point.

can be written as the sum of two components, a resonant component $\sigma_{\rm i}^{\rm R}(\sqrt{s})$ arising from Z decays, and a non resonant one $\sigma_{\rm i}^{\rm NR}$, interpreted as the two-photon background. Since only for energies below $E_{\rm lim} = 25\%\sqrt{s}$ the background from two-photon processes is expected to contribute, this determines the integration interval used to define the total non-resonant cross section: $\sigma^{\rm NR}(\sqrt{s}) = \sum_{\rm i} \sigma_{\rm i}^{\rm NR}(\sqrt{s})$ with $E_{\rm TPC}^{\rm i}<E_{\rm lim}$. The region above $E_{\rm lim}$ where the two-photon background is expected to be negligible defines the purely resonant cross section $\sigma^{\rm R}(\sqrt{s})$. For each $\sqrt{s}$, the cross section $\sigma_{\rm i}$ can be related to the resonant component $\sigma^{\rm R}$ via the equation

$$\sigma_{\rm i} = \sigma_{\rm i}^{\rm NR} + \frac{\sigma_{\rm i}^{\rm R}}{\sigma^{\rm R}}\sigma^{\rm R}. \tag{7}$$

As shown in Figure **??**, a straight-line fit in the plane ($\sigma_{\rm i}$,$\sigma^{\rm R}$) yields a constant term which is identified as the two-photon background in energy bin i, so that the total non resonant background is obtained from the sum $\sigma^{\rm NR} = \sum_{\rm i} \sigma_{\rm i}^{\rm NR}$ in the interval (0.1–0.25)$\sqrt{s}$.

Figure 6: Hadronic cross section in the charged energy interval i as a function of those in the interval (0.25–1)$\sqrt{s}$ at different centre-of-mass energies

The uncertainty in the extrapolation to full acceptance coming from the hadronization models has been evaluated for each energy point using the technique already described in [17].

Events centrally produced ($| \, cos\theta_{\mathrm{thrust}} \, | \, < \, 0.2$) are rotated randomly in space and their acceptance calculated by reweighing the events by the proper thrust angular distribution. The same procedure is applied to fully simulated events and a difference in efficiency of 0.07% is measured. This comparison leads to a better agreement now than in previous studies [17] by a factor of 2, essentially due to a more accurate simulation of low p_t tracks in the Monte-Carlo. The same study has been repeated for the different scan points and no dependence was observed as a function of $\sqrt{s}$. However, since low charged multiplicity events are not contained in the rotated sample, this procedure does not check how well this class of events is reproduced in the simulation. To verify this, $\mathrm{q\overline{q}}$ events are selected by a cut on the charged multiplicity in one of the two event hemispheres as defined by a plane perpendicular to the thrust axis. Good agreement between data and Monte Carlo is observed in the opposite hemisphere for low multiplicity events as shown in Fig. 7. A conservative systematics of 0.02% is assigned after having verified that multiplicities in the two hemispheres are uncorrelated at first order. The improvement in the simulation of low energy tracks also leads to a better agreement on the selection variables between data and Monte Carlo reducing this source of systematics to 0.02%.

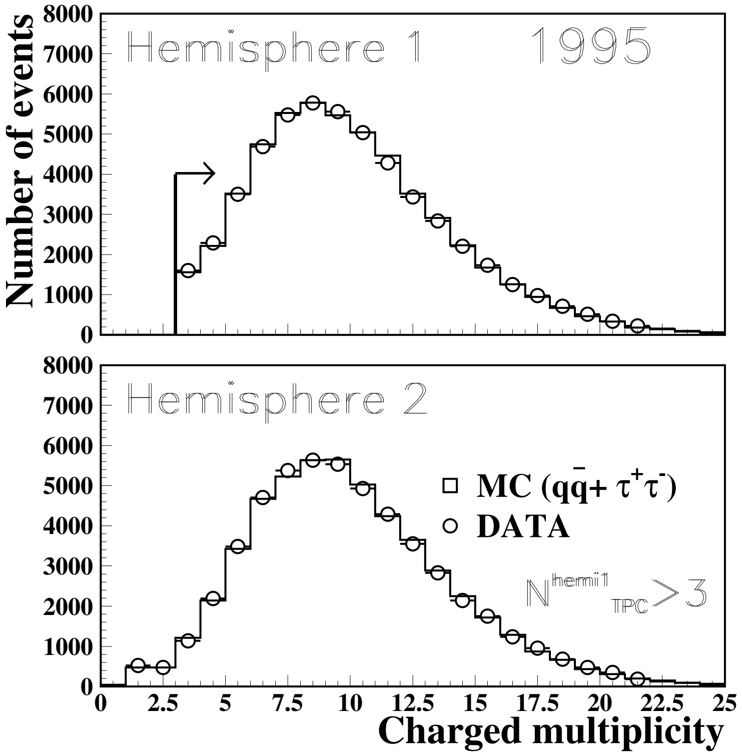

Figure 7: Distribution of charged multiplicity in data and Monte Carlo. The cut $N_{\mathrm{TPC}} > 3$ is applied in hemisphere 1 and the comparison between data and Monte Carlo is performed in hemisphere 2.

Combining all the errors assigned to detector response, Monte-Carlo , background and modelling gives a total systematic error for the track based selection of 0.0xx% at the peak energy, therefore improving with respect to [17] by almost a factor 2.

The background contamination and the various contributions to the systematic error are summarised in table 9.

8.0.2 The calorimetric selection

The other, independent, event selection uses calorimetric data to select hadronic Z decays with an acceptance slightly larger compared to the track based selection. Events are required to have ECAL energy measured with the wire readout of at least 7 GeV in the barrel or 1.5 GeV in each end-cap, as well as a combined ECAL and HCAL energy of at least 20% of the centre-of-mass energy. These cuts, as will be seen, reduce two-photon event rates to a negligible level. A time window of ± 100 nsec, measured on ECAL signals, removes the bulk of cosmic-ray background. Additional requirements are imposed on events with less than five good charged particle tracks to suppress the background from lepton pairs.

- Bhabha events are removed on the basis of their large localised energy deposition in the ECAL: the two most energetic ECAL clusters of the events are required to be less than 35 and 25 GeV, respectively. Two particular angular regions, the area of overlap between barrel and endcap, where the energy resolution is degraded, and the low angle area, where part of the event may be lost due to ECAL geometrical acceptance, need more care. For these regions, the additional requirement is made that the summed energy of the two main ECAL clusters be less than 84% of the total calorimetric energy.
- Z$\rightarrow \tau^+\tau^-$ events are removed by their characteristic collimated back-to-back jet structure. The calorimetrically measured thrust value must be less than 0.996 and the minor value of the energy tensor must be larger than 0.03. After these cuts the remaining τ-pair background, estimated with simulated data, is small (????%) and a correction is made to the cross section.
- Z$\rightarrow \mu^+\mu^-$ decays, which pass the initial calorimetric cuts because they have a radiated photon, are eliminated by rejecting events with exactly two tracks, each with four or more associated hits in the outer ten layers of the HCAL. The remaining μ-pair background is negligible.
- Remaining cosmic-ray background in time with the beam is removed in the following way. Events with exactly one track are rejected unless this track projects to the vertex cylinder, which is 2 cm in radius and ± 20 cm along the beam direction. Events are also rejected if there are less than two ECAL clusters of more than 3 GeV. The residual cosmic-ray contamination is calculated on the basis of the properties of the events outside the timing window.

Events from two-photon processes are suppressed very efficiently by the preselection. Possible remaining background has been estimated using the events with between ?? and ?? of calorimetric energy, where the two photon events concentrate. The same method is used as

for the track-based selection and at most ?? pb remain in the sample.
The remaining Bhabha background is studied in a similar way. As it is concentrated at small angles, an enriched sample is obtained by selecting events with less than five tracks and $\cos\theta|>0.95$ and compared with the full sample as a function of the beam energy. Here, the background term consists not only of the non-resonant photon exchange, but also of the Z exchange and interference between them. An estimated background of ??? pb is removed from the cross section calculation.

9 Measurement of the leptonic cross sections

9.1 Muon event selection

The muon-pair events are selected in three steps. First, a preselection is performed based on the tracking information to select events with low charged particle tracks multiplicity and at least one high momentum track. In detail, the following cuts are imposed on good charged particle tracks.

- The event is retained if it has two to eight charged tracks.
- The two highest momentum tracks must have $|\cos\theta| \leq 0.95$ and $|\cos\theta^*| \leq 0.90$.
- The two highest momentum tracks must have opposite charge.
- The sum of the momenta of the two leading tracks must be less than $1.5\sqrt{s}$.
- The sum of the number of ITC hits associated to the two leading tracks must be at least two.
- For the two leading tracks it is required that $|d_0| < 2\,\mathrm{cm}$ and $|z_0| < 5\,\mathrm{cm}$.
- The momentum of the leading track p_1 must be larger than $35\sqrt{s}/91.2$.

Hadronic Z decays and background from two-photon interactions are reduced to a negligible level after this first series of requirements. Then, photons identified in ECAL are added to the tracking information to retain only those events compatible with a $\mu^+\mu^-(\gamma)$ topology. An event is selected as a muon-pair candidate if at least one of the following requirements is fulfilled:

- The momentum of the second fastest track p_2 exceeds $35 \times \sqrt{s}/91.2$ and the acollinearity η is less than 20°.
- η is less than 10 mrad.
- A photon is found in the ECAL acceptance, i.e., $|\cos\theta_\gamma| < 0.98$, which is consistent in energy and position with a $\mu^+\mu^-\gamma$ hypothesis. This requires that the measured photon energy $E_{\gamma\mathrm{meas}}$ be equal to the expected one $E_{\gamma\mathrm{exp}}$ within four times the estimated photon

energy resolution $\sigma_{E_\gamma} = 20\%\sqrt{E_{\gamma\text{meas}}}$. The expected photon energy $E_{\gamma\text{exp}}$ is obtained from the directions of the two leading charged tracks and of the photon by imposing energy and momentum conservation

$$E_{\gamma\text{exp}} = \frac{\sqrt{s}\sin\theta_{\mu^+\mu^-}}{\sin\theta_{\mu^+\mu^-} + \sin\theta_{\mu^+\gamma} + \sin\theta_{\gamma\mu^-}}.$$

In addition the angle between the photon and the closest of the two leading tracks must be larger than 30 mrad and the event must be contained in a plane. The sum of the photon energy and of the momenta of the two leading tracks is required to exceed $0.85 \times \sqrt{s}$.

The effect of the p_2 and $\eta < 20^\circ$ cuts is to reject those events with initial state photon radiation (ISR) larger than 0.25-0.30 $E_{\text{beam}} \simeq 12$ GeV, as shown in Fig. 8. The $\eta < 10$ mrad cut

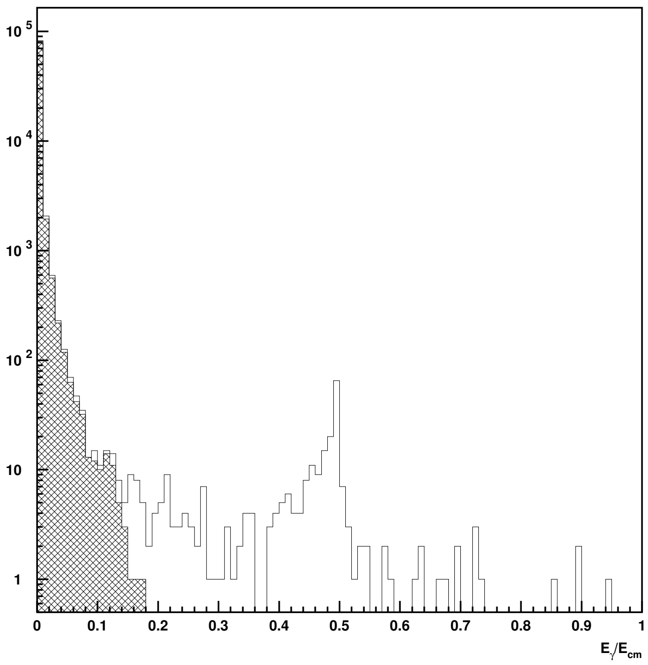

Figure 8: Distribution of the total photon energy emitted along the beam pipe before (white histogram) and after (hatched histogram) the momentum, acollinearity and $\cos\theta^*$. The plot is based on Monte Carlo events generated at the peak point.

recovers events with final state radiation (FSR) when the emitted photon is almost collinear with respect to one of the two muons and energetic enough for the muon momenta to be rejected by the p_1, p_2 cuts. The request of consistency with a $\mu^+\mu^-\gamma$ hypothesis is designed to improve the efficiency for events with FSR if the photon is identified and its energy well measured. Figure 9 shows the effect of the momentum and acollinearity cuts in the $\theta_{\gamma\mu^+}$ vs $\theta_{\gamma\mu^-}$ plane, where $\theta_{\gamma\mu^+}$ and $\theta_{\gamma\mu^-}$ are the angles between the photon and the μ^+, μ^-.

Figure 9: Representation of the momentum and acollinearity cuts in the $\theta_{\gamma\mu^+}$ vs $\theta_{\gamma\mu^-}$ plane, in the hypothesis of only one emitted photon in the final state. Region 1 is not allowed due to momentum conservation. Region 3 is excluded by the momentum cut (at least one track with momentum larger than $35\sqrt{s}/91.2$). In region 2 events are accepted by the momentum and $\eta < 20°$ cuts, without an explicit photon search. Finally, region 4 requires the identification of a photon and the consistency with the $\mu^+\mu^-\gamma$ hypothesis.

Finally, at least one of the two leading momentum tracks must be identified as a muon on the basis of the HCAL and muon chambers digital readout.

- The track must have at least one associated muon chamber hit.
- Alternatively, the track must penetrate into the iron of the HCAL, that is, the following conditions must be fulfilled: $N_{\rm fire}/N_{\rm exp}>0.5$, $N_{\rm exp} \geq 10$, and $N_{10}/N_{\rm exp10}>0.3$, where $N_{\rm fire}$, $N_{\rm exp}$ and N_{10} and $N_{\rm exp10}$ are, respectively, the number of actually firing planes, the number of planes expected for the track, the number of firing planes within the ten outermost expected, and the number of expected planes within the ten outermost ones.

The muon identification cuts effectively separate the $\mu^+\mu^-$ pairs from the e^+e^- pairs and reduce the tau background down to a $\gtrsim 0.2\%$ level. The acceptance of the selection after all cuts except muon identification, $\varepsilon_{\rm acc}$, is evaluated from fully reconstructed Monte Carlo events generated with KORALZ 4.0. Table 10 shows the value of the acceptance as a function of the cuts applied after preselection for the different energy points. The preselection requirements include the condition $|\cos\theta^*| \leq 0.90$ which, assuming an angular distribution proportional to $1+\cos^2\theta^*$, by itself reduces the acceptance to 85.725%. The results reported in Table 10 indicate a small dependence of the acceptance on centre-of-mass energy, as already found for hadrons. Since the Monte Carlo samples were generated at energies slightly different from the LEP energies, the acceptances for the off-peak points are corrected by interpolating the Monte Carlo acceptances with straight lines.

Energy	$\varepsilon_{p_2>35\sqrt{s}/91.2\,{\rm GeV}/c}$	$\varepsilon_{\eta<10\,mrad}$	$\varepsilon_{\mu\mu\gamma}$	$\varepsilon_{\rm acc}$
peak−3	$79.45 \pm 0.18\%$	$0.71 \pm 0.04\%$	$2.16 \pm 0.07\%$	$82.322 \pm 0.171\%$
peak−2	$80.24 \pm 0.18\%$	$0.80 \pm 0.04\%$	$2.26 \pm 0.07\%$	$83.308 \pm 0.167\%$
peak−1	$80.62 \pm 0.18\%$	$0.83 \pm 0.04\%$	$2.35 \pm 0.07\%$	$83.794 \pm 0.165\%$
peak	$80.98 \pm 0.05\%$	$0.81 \pm 0.01\%$	$2.29 \pm 0.02\%$	$84.078 \pm 0.048\%$
peak+1	$80.61 \pm 0.18\%$	$0.73 \pm 0.04\%$	$2.29 \pm 0.07\%$	$83.626 \pm 0.165\%$
peak+2	$80.20 \pm 0.18\%$	$0.70 \pm 0.04\%$	$2.07 \pm 0.06\%$	$82.964 \pm 0.168\%$
peak+3	$79.79 \pm 0.18\%$	$0.56 \pm 0.03\%$	$1.89 \pm 0.06\%$	$82.240 \pm 0.171\%$

Table 10: Details of the acceptances after preselection. The fractions of events in columns two and three should be understood as the fractions of events which do *not* pass the selections of the preceding columns and pass that of the considered column. The acceptances given in column five, $\varepsilon_{\rm acc}$, are obtained as the sum of the three preceding columns.

The muon identification efficiency is measured with data by comparing the number of events that have both sides identified (N_2) with the number of events with only one side identified (N_1). In the approximation of no correlations between the two muons in an event and no background, the following relations hold

$$\begin{aligned} N_2 &= N\varepsilon_\mu^2 \\ N_1 &= 2N\varepsilon_\mu(1-\varepsilon_\mu), \end{aligned}$$

where ε_μ is the (mean) muon identification efficiency for a single track and N is the unknown number of $e^+e^- \to \mu^+\mu^-$ events produced. Since an event is accepted if at least one of the two tracks is identified as a muon, the event efficiency results to be

$$\varepsilon_{\mu\mu} = 1-(1-\varepsilon_\mu)^2 = \frac{4N_2(N_2+N_1)}{(2N_2+N_1)^2}.$$

Correlations in the identification efficiency between the two muons introduced by the presence of inactive zones in the HCAL or muon chambers are evaluated with the $\mu^+\mu^-$ Monte Carlo. A correlation coefficient $\kappa = (0.318 \pm 0.020)10^{-3}$ is obtained and a correction applied to the efficiencies evaluated at each energy point $\varepsilon_{\mu\mu}^{\text{corr}} = (1+\kappa)\varepsilon_{\mu\mu}$.

Since N_1 and N_2 are determined from data applying all cuts except muon identification, a bias to the efficiency measurement could be induced by the presence of a residual $\tau^+\tau^-$ contamination which, from Monte Carlo, is estimated to be $\simeq 3.710^{-4}$ for N_2 and $\simeq 5.3\%$ for N_1. To reduce this residual background, an additional selection is applied based on the presence of minimum ionising particle signals in ECAL and HCAL. From data, the variations of the identification efficiencies associated to this $\tau^+\tau^-$ contamination are measured to be $\Delta\varepsilon_\mu = (-8.4 \pm 0.5) \cdot 10^{-4}$ and $\Delta\varepsilon_{\mu\mu}^{\text{corr}} = (-4.1 \pm 0.3) \cdot 10^{-5}$, in good agreement with those estimated with simulated events. After all corrections, the mean identification efficiencies are measured to be $\varepsilon_\mu = 0.9763 \pm 0.0003$ and $\varepsilon_{\mu\mu}^{\text{corr}} = 0.99976 \pm 0.00001$. The variation of $\varepsilon_{\mu\mu}^{\text{corr}}$ as a function of time, with and without the calorimetric filter is shown in Figure 10. A slight inefficiency can be observed for the 1990 data, when only one double-layer of muon chambers was installed, and for the 1993 prescan point, when both muon chamber double-layers in the region $\Delta\phi = 30°$, $|\cos\theta| < 0.67$ were not operational due to a hardware failure.

The most important source of background originates from $e^+e^- \to \tau^+\tau^-$ events and is measured to be $(2.24 \pm 0.05)10^{-3}$ at the peak from Monte Carlo simulation. At peak+2 and peak-2, the $\tau^+\tau^-$ background estimates are $(2.04 \pm 0.10)10^{-3}$ and $(1.86 \pm 0.14)10^{-3}$, respectively. These estimates are used to correct the number of selected events at different centre-of-mass energies: the contamination at the peak is used for the data at the peak and peak$\pm$1, while the contamination at peak$\pm$2 is used for the peak$\pm$2 and peak$\pm$3 points. The background from electron-pair is also estimated from simulated events and found to be negligible. Cosmic-ray events are rejected both by the cuts on the distance of closest approach of the tracks to the collision point and also by the explicit requirement on the number of ITC hits. In fact, the ITC hits are reconstructed only if the drift time is within a certain time window with respect to the beam crossing signal and the same is true for the ITC trigger signals used by the muon track trigger. This residual cosmic-ray contamination is estimated for each energy point by loosening the vertex requirements and using the number of additional events found to estimate the number of background events accepted by the standard vertex requirements. The resulting background averaged over all energy points is $\simeq 410^{-4}$.

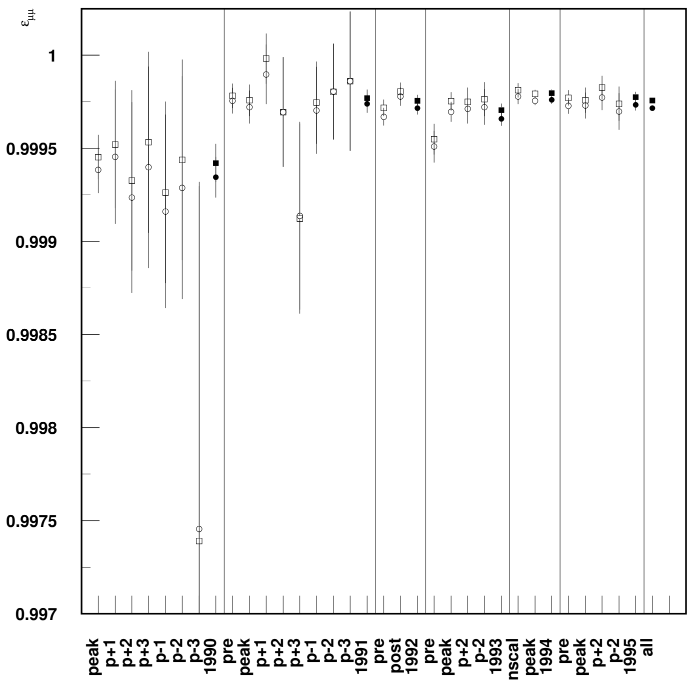

Figure 10: Measured $\mu^+\mu^-$ identification efficiency for the different data-taking periods with (squares) and without (circles) the calorimetric filter. The black points indicate the average efficiency for each year.

9.2 Tau event selection

The design of the tau event selection is mainly based on the following features of $\tau^+\tau^-$ events: the clean back-to-back topology due to the high Lorentz boost in tau decays, the low charged track multiplicity, and the presence of undetected neutrinos. The following energy flow objects are used in the definition of the selection criteria

- good charged tracks having $|d_0| < 2$ cm and $|\cos\theta| < 0.95$;
- photons with energy greater than 1 GeV;
- neutral hadrons with energy greater than 1.5 GeV.

The minimal energy requirement for the neutral calorimeter objects is introduced in order to be less sensitive to shower fluctuations (not properly simulated in the Monte Carlo), and therefore to reduce related systematic effects.

In order to select tau-pairs events, a preselection is applied to define the geometrical acceptance and to reject most of hadronic and two-photon events. Events are retained if

- there is at least one good charged track per hemisphere;
- the total number of charged tracks does not exceed eight;
- the scattering angle satisfies the requirement $|\cos\theta^*| < 0.9$;
- the acollinearity η is less than $20°$.

Additional reduction of the background due to two-photon interactions is obtained by requiring either the total reconstructed energy, $\mathrm{E_{rec}}$, to be larger of $0.175\sqrt{\mathrm{s}}$ or the absolute difference between the transverse momenta of the jets to be greater than $0.033\sqrt{\mathrm{s}}$ ("$\gamma\gamma$ cuts").

The contamination from hadronic Z decays is further reduced by applying additional cuts ("hadronic cuts") on events in which both hemispheres have either more than one charged track or an invariant mass greater than 0.8 $\mathrm{GeV/c^2}$ or the invariant mass of the opposite hemisphere greater than 3 $\mathrm{GeV/c^2}$. Defining $\mathrm{N_{obj,i}}$ and $\theta_{\mathrm{i}}^{\mathrm{op}}$ and as the number of charged and neutral objects and the maximum angle between two charged tracks in hemisphere i, respectively, events are retained if $\prod_i \mathrm{N_{obj,i}} < 50$ and $\sum_i \theta_{\mathrm{i}}^{\mathrm{op}} < 0.30$ rad. Moreover, for events with 1 (> 1) charged tracks in one of the two hemispheres, the minimum invariant hemisphere mass $\min(\mathrm{m_i})$ should be below 3 $\mathrm{GeV/c^2}$ (< 1.8 $\mathrm{GeV/c^2}$).

Cosmic ray rejection is obtained by requiring at least one charged track to originate from within a cylinder of length 5 cm and radius 1 cm coaxial with the beam and centred on the measured collision point.

Bhabha and dimuon events are rejected in two steps. First, a common cut is applied on the sum of the momenta of the two leading charged tracks, required to be in excess of $80\%\sqrt{\mathrm{s}}$ ("leading momenta cut"). Then, lepton identification is used to define bhabha-like and dimuon-like events as follows. The electron definition is extended to include charged tracks pointing less than 3 cm away from ECAL insensitive regions: these are always called electrons unless they are positively identified as muons. An event is then called bhabha-like if all the charged tracks are identified as electrons. The fractions of $\mathrm{e^+e^-}$ and $\tau^+\tau^-$ events being tagged as bhabha-like at this level are 99.5% and 8%, respectively. The dimuon-like definition requires either both leading charged tracks being identified as muons or one leading charged track identified as muon and the energy in the opposite hemisphere in excess of $45\%\sqrt{\mathrm{s}}$. The fractions of $\mu^+\mu^-$ and $\tau^+\tau^-$ events being tagged as dimuon-like at this level are 98.8% and 7%, respectively.

Bhabha and dimuon rejection is achieved by applying total energy related cuts to bhabha-like ("bhabha cuts") and dimuon-like ("dimuon cuts") events. The total energy $\mathrm{E_{tot}}$ is defined as $\mathrm{E_{rec}} + \mathrm{E_{rad}}$, where $\mathrm{E_{rec}}$ is the total reconstructed energy and $\mathrm{E_{rad}}$ is the energy of a photon collinear to the beam computed using the jet directions and imposing 4-momentum conservation. Possible losses of photons due to ECAL insensitive regions are tagged using the variables $\mathrm{D_{g,i}}$ defined by taking the tangents to the leading tracks in each hemisphere at the origin, extrapolating them to ECAL, and computing their minimum distance from ECAL insensitive regions. Bhabha rejection is obtained by applying a staggered cut in the variables $\mathrm{D_{min}} = \min(\mathrm{D_{g,i}})$ and $\mathrm{E_{tot}}$: events are retained if $\mathrm{E_{tot}} < 0.8\sqrt{\mathrm{s}}$ when $\mathrm{D_{min}} > 6$ cm, or $E_{tot} < 0.7\sqrt{s}$ when $D_{min} < 6$ cm. Dimuon rejection is obtained by requiring $\max_E = \max(P_{l,1}, P_{l,2}, E_{tot}/2) < 0.45\sqrt{s}$, where $P_{l,i}$ are the leading momenta.

The background fractions from different sources are reported in table 11. These numbers are estimated using data and Monte Carlo simulations as described below.

The number of Bhabha events (N_{bha}^{lead}) passing the leading momenta cut is obtained by counting the number of bhabha-like events with $E_{tot} > 0.25\sqrt{s}$ and correcting for the $\tau^+\tau^-$ contamination and for the inefficiency of the E_{tot} cut using, respectively, the $\tau^+\tau^-$ and e^+e^- Monte Carlo. The efficiency of the bhabha-like definition on Bhabha events (P_{bha}) is extracted from data by counting the number of events with 0, 1 or 2 bhabha-like hemispheres (i.e., having all charged tracks in a hemisphere identified as electrons) in the sample with $E_{tot} > 0.95\sqrt{s}$, assuming the hemispheres uncorrelated; the Bhabha Monte Carlo is used to calculate the small correction to P_{bha} due to the correlation between hemispheres. The fraction of Bhabha-like events satisfying the E_{tot} cut, $f_{E_{tot}}$, is evaluated fitting the data with the Monte Carlo distributions for $\sin\eta$, an observable which allows to separate the e^+e^- and $\tau^+\tau^-$ components. The result of the fit for the 1994 data is shown in figure 11a. The number of background events after all cuts is calculated from the expression

$$N_{bha}^{bkg} = N_{bha}^{lead}\left(\frac{1 - P_{bha}}{P_{bha}} + f_{E_{tot}}\right).$$

A similar procedure is applied to estimate the dimuon contamination. The efficiency of the final $\max_E$ cut is taken from Monte Carlo. The $\max_E$ distribution before the last cut is shown for the 1994 data in Figure 11b.

The hadronic background is estimated from Monte Carlo; the overall normalization is checked before the cut on the minimum hemisphere invariant mass by fitting the data with the relevant reference distributions of ditau and hadronic Monte Carlo events; as an example, Figure 11c shows the result of the fit for the 1994 data; the agreement is at the 10% level. The reference distributions are checked using an artificial sample of hadronic events obtained by tagging hadronic hemispheres using the information of the opposite hemisphere only, and then pairing tagged hadronic hemispheres. The systematic effect due to bad simulation is estimated to be less than 10%.

The background from two-photon processes is estimated from Monte Carlo. The $\gamma\gamma \rightarrow$ hadrons contribution is expected to be negligible. Therefore, the Monte Carlo normalization is checked using enriched samples of $\gamma\gamma \rightarrow$leptons events. The overall agreement is at 10% level. The acollinearity distribution for the events satisfying all the remaining selection cuts is shown for the 1994 data in Figure 11d.

The number of cosmic events satisfying the selection cuts is estimated from the data by applying all selection cuts except those against cosmic rays, and looking at the distribution of the minimum d_0 of the two leading tracks; the contamination is derived assuming such a distribution to be flat. The larger contamination for the 1995 run is due to different timing conditions needed to cope with LEP running in bunch-trains mode.

Source	Fraction (%)
e^+e^-	0.69 ± 0.11
$\mu^+\mu^-$	0.09 ± 0.05
$q\overline{q}$	0.29 ± 0.04
2-photon	0.26 ± 0.03
Cosmic rays (95)	0.014 ± 0.001 0.040 ± 0.009
Total (95)	1.34 ± 0.12 1.37 ± 0.12

Table 11: Sources of contamination to the $\tau^+\tau^-$ selected sample and their average fraction at the peak.

The bulk of the $\sqrt{s}$ dependence of the Bhabha, hadronic and dimuon background is taken into account automatically by the normalization on data. When needed, the remaining dependence is taken into account with the Monte Carlo. For two-photon processes a constant cross section is assumed over the $\sqrt{s}$ range considered. The average total background fractions for the off-peak points are reported in Table 12.

$\sqrt{s}$	Fraction (%)
peak-3	5.12 ± 0.38
peak-2	2.96 ± 0.21
peak-1	1.91 ± 0.16
peak+1	1.33 ± 0.12
peak+2	1.85 ± 0.13
peak+3	2.35 ± 0.19

Table 12: Average background fractions for off-peak points.

The total efficiency can be written as $\epsilon_{\tau\tau} = \epsilon_{\rm trig} \cdot \epsilon_{\rm acc} \cdot \epsilon_{\rm sel}$ where $\epsilon_{\rm trig}$ is the trigger efficiency discussed in Section 3.1, $\epsilon_{\rm acc}$ is the geometrical acceptance defined by the preselection cuts, and $\epsilon_{\rm sel}$ is the selection efficiency inside the acceptance.

The acceptance is taken from Monte Carlo. Systematic effects related to distorsions or detector misalignment are investigated using toy Monte Carlo techniques; a maximum shift of $3 \cdot 10^{-4}$ is obtained. The level of simulation of TPC tracking inefficiencies is checked using e^+e^- and $\tau^+\tau^-$ events; the Monte Carlo is found to reproduce the data at the level of $3 \cdot 10^{-4}$. The propagation of the uncertainity on the TPC drift velocity is found to be negligible. To account for these effects, a systematic error of $4 \cdot 10^{-4}$ is added in quadrature to the Monte Carlo statistical error. To take into account the different detector configuration in 1990, a dedicated Monte Carlo simulation is used to evaluate the acceptance for that year. The values of $\epsilon_{\rm acc}$ at the peak for different years of data-taking are given in table 13. The dependence of $\epsilon_{\rm acc}$ on centre-of-mass energy is studied with high statistics Monte Carlo samples processed through a fast and simplified detector simulation. The correction factors to be applied to the acceptance calculated at the peak are given in table 14.

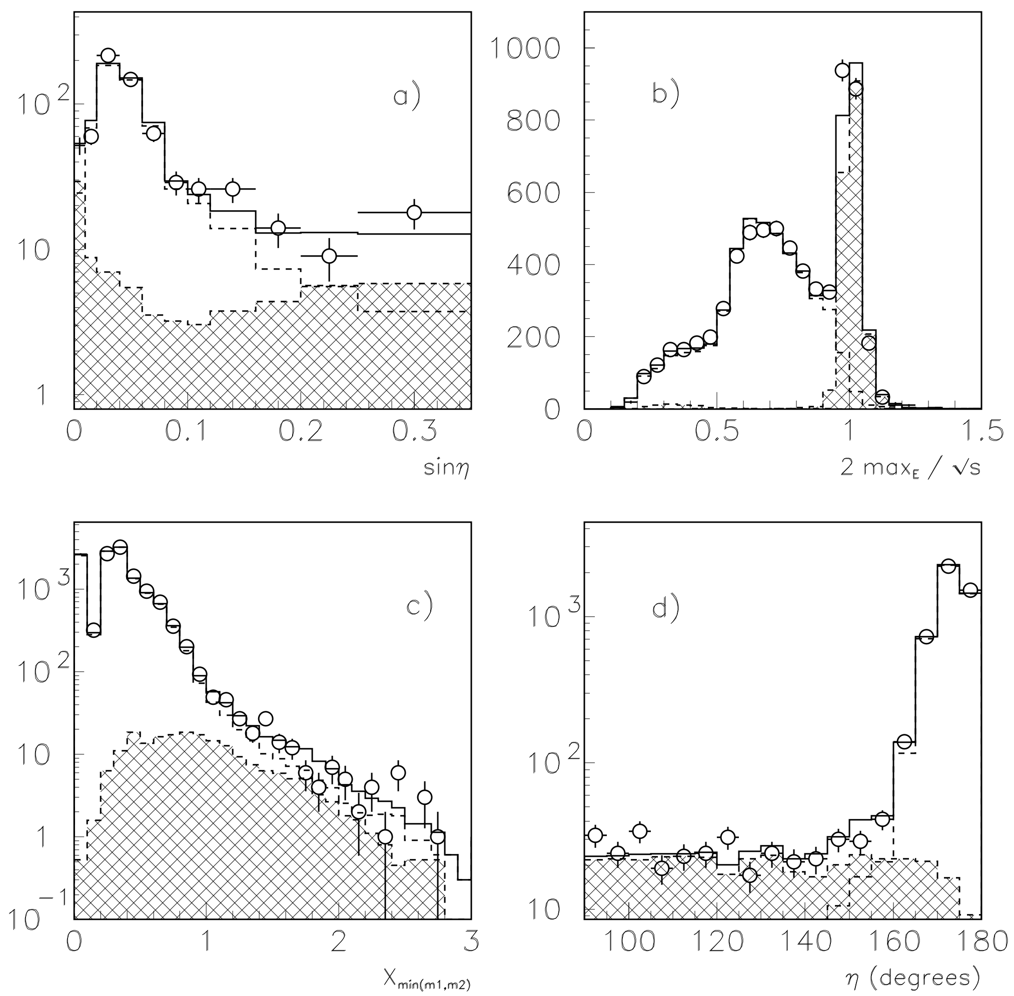

Figure 11: Distribution of some variables used in background studies to the tau selection; see text for the description of the variables. In all figures, circles with error bars are 1994 data, the dashed histogram is the ditau Monte Carlo, and the crossed-hatched histogram is the Monte Carlo for Bhabhas (a), dimuons (b), hadronic Z decays (c), and two-photon into leptons (d).

The selection efficiency can be written as $\epsilon_{\rm sel} = \epsilon_{\gamma\gamma} \cdot \epsilon_{\rm had} \cdot \epsilon_{\rm lead} \cdot \epsilon_{\rm bha} \cdot \epsilon_{\rm muo}$ where $\epsilon_{\gamma\gamma}$, $\epsilon_{\rm had}$, $\epsilon_{\rm lead}$, $\epsilon_{\rm bha}$, and $\epsilon_{\rm muo}$ are, respectively, the efficiencies of the $\gamma\gamma$ cuts, hadronic cuts, leading momenta cut, bhabha and dimuon cuts. According to the Monte Carlo, the cut against the cosmic-ray background has a negligeable effect on the signal.

The selection efficiency is studied from data in two ways. The first method uses artificial tau pairs. A $\tau^+\tau^-$ selection based on the information of one hemisphere only is designed to select an almost unbiased sample of tau hemispheres. The selected hemispheres are then paired to form artificial $\tau^+\tau^-$ events from which $\epsilon_{\rm sel}$ is obtained. To estimate a possible bias to this measurement the procedure is repeated with $\tau^+\tau^-$ Monte Carlo events, leading to a shift on $\epsilon_{\rm sel}$ of $+(2.9 \pm 0.7) \cdot 10^{-3}$ with respect to the determination based on data. The main systematic uncertainty arises from the background contamination to the selected sample of tau hemispheres, which is measured using the techniques already described. To study the impact of such background on the selection efficiency, the measured proportion of background Monte Carlo events is introduced into the $\tau^+\tau^-$ Monte Carlo and the artificial tau-hemispheres pairing is applied to the sample obtained. The main contamination arises from hadronic Z decays. The total correction to the selection efficiency amounts to $(+5.5 \pm 1.3) \cdot 10^{-3}$.

The second method compares the number of events rejected by a given set of cuts in data and Monte Carlo. All selection cuts, except the ones under study, are applied, but some additional requirements are introduced to increase the purity of the sample and to reduce the systematic uncertainty associated to background subtraction. The number of background events is extracted by fitting the data to the Monte Carlo distributions of the relevant processes, and it is subtracted from the number of data rejected by the cuts only; the number obtained in this way is compared to the ditau Monte Carlo prediction. The systematic uncertainty is evaluated by changing the range used to fit the background content.

Both techniques give a measurement of the agreement between data and Monte Carlo for the inefficiency introduced by the cuts. The two methods give results in agreement between each other, and are combined to give the best estimate, cut by cut, of the level of the simulation. The inefficiencies predicted by the Monte Carlo are then corrected for the ratios measured, and the precision of the test is added in quadrature as systematic error. The procedure is applied to the data collected at the peak; the resulting values for the selection efficiency are in good agreement among the data sets taken in different years, and are combined to give the value shown in table 13.

The $\sqrt{s}$ dependence of the selection cuts efficiency is studied with simulated events. A non negligeable variation is found for $\epsilon_{\rm had}$, coming from the variation of the hemisphere invariant mass distribution with $\sqrt{s}$ due to the different amount of final state radiation. The size of the effect is checked on data using the artificial tau pairs method, and found in agreement with the Monte Carlo prediction. The correction factors to be applied to the peak value are given in table 14. A systematic error of 20% of the correction has been conservatively added in quadrature to the Monte Carlo statistical error.

9.3 Electron event selection

The selection of wide-angle Bhabha events is made based solely on kinematic cuts. Since the event topologies are relatively unique, particle identification is only required for event rejection. The selection procedure demands the following criteria to be satisfied.

- Events are required to have either exactly two good tracks or three to six good tracks which satisfy a more restrictive d_0 requirement ($|d_0| < 2$ cm). There should be at least one track in each event hemisphere.

	Acceptance	
	1990	1991-1995
$\epsilon_{\rm acc}$	0.82800 ± 0.00189	0.82407 ± 0.00056
	Selection	
Term	Data corrected	MC value
$\epsilon_{\gamma\gamma}$	0.98805 ± 0.00061	0.98876 ± 0.00011
$\epsilon_{\rm had}$	0.97879 ± 0.00098	0.97943 ± 0.00015
$\epsilon_{\rm lead}$	0.99405 ± 0.00042	0.99435 ± 0.00008
$\epsilon_{\rm bha}$	0.99297 ± 0.00043	0.99292 ± 0.00009
$\epsilon_{\rm muo}$	0.99211 ± 0.00043	0.99199 ± 0.00009
$\epsilon_{\rm sel}$	0.94673 ± 0.00135	0.94845 ± 0.00023
	Trigger	
$\epsilon_{\rm trig}$	0.999965 ± 0.000002	
	Global	
	1990	1991-1995
$\epsilon_{\tau\tau}$	0.7839 ± 0.0021	0.7802 ± 0.0012

Table 13: Acceptance, selection and total efficiencies at the peak for the different data taking periods. Shown are: the acceptance values used for 1990 data and for the remaining data; the values for the cut efficiencies obtained after correcting the Monte Carlo values using the data (see text) compared to the original Monte Carlo values; the global efficiencies values used for 1990 peak data and for the remaining peak data.

$\sqrt{s}$	Acceptance	Selection
peak-3	0.9840 ± 0.0022	0.9963 ± 0.0015
peak-2	0.9936 ± 0.0012	0.9990 ± 0.0007
peak-1	0.9982 ± 0.0021	0.9999 ± 0.0003
peak+1	1.0008 ± 0.0021	0.9990 ± 0.0003
peak+2	0.9949 ± 0.0012	0.9968 ± 0.0008
peak+3	0.9906 ± 0.0022	0.9944 ± 0.0014

Table 14: Correction factors to take into account the acceptance and selection efficiency dependence on the center-of-mass energy.

- At least one track with $|d_0|$ less than 2 cm is required to have a momentum exceeding 3 GeV/c.
- If four or more good tracks are measured, then each of them is required to have an opening angle ξ with respect to the axis of the corresponding jet which fulfils $\cos(\xi) > 0.85$.
- The acollinearity is required to be 20° or less.

The requirements described so far serve mainly for the suppression of hadronic final states, two-photon interactions and background from cosmic rays and beam-gas interactions. In order to reject $\mu^+\mu^-$ and $\tau^+\tau^-$ final states, additional cuts are introduced, based on the momenta of the selected tracks and on the ECAL energies associated to these tracks. The possible loss of electromagnetic energy due to radiated photons is corrected for, as is the energy which escapes through insensitive regions of the ECAL, but is recovered by the HCAL. In detail the requirements are the following:

- The sum of the two highest momentum tracks is required to be greater than $0.05\sqrt{s}$ ('Σp cut').
- The sum of the two ECAL energies associated to the two highest momentum tracks is required to exceed $0.20\sqrt{s}$ ('ΣE cut').
- The total sum of the two highest momentum tracks plus energies after all corrections is required to be larger than $1.20\sqrt{s}$ ('Σp+$\Sigma\mathcal{E}$ cut').
- The two highest momentum tracks should not be identified as muons.

A comparison between data and Monte Carlo for the Σp+$\Sigma\mathcal{E}$ variable, which defines the most stringent cut, is shown in Fig. 12.

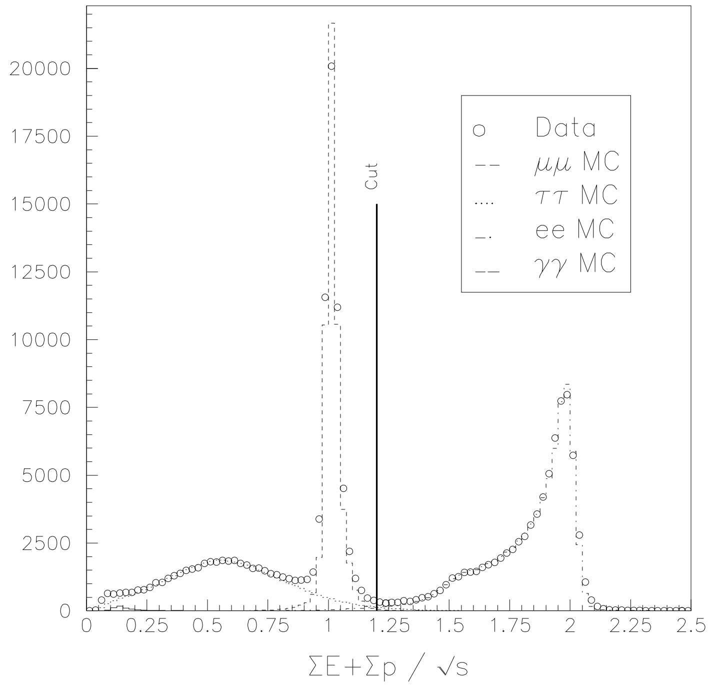

Figure 12: 'Σp+$\Sigma\mathcal{E}$' cut for lepton pairs, together with Monte Carlo predictions for the different lepton species.

The signal efficiency is evaluated using several samples of Bhabha events generated with the UNIBAB Monte Carlo generator [9]. This efficiency is seen to be essentially flat over much of the angular range of interest with an expected small tail-off at large values of $|\cos\theta^*|$. These results are illustrated in Figure 13. The efficiency within the angular ranges $-0.9 <$

$\cos\theta^* < +0.7$, $\eta < 20°$ is calculated to be 0.9890±0.0002 at the peak and ranges, in value, from 0.9883±0.0027 (Peak+2) to 0.9904±0.0013 (Peak+1).

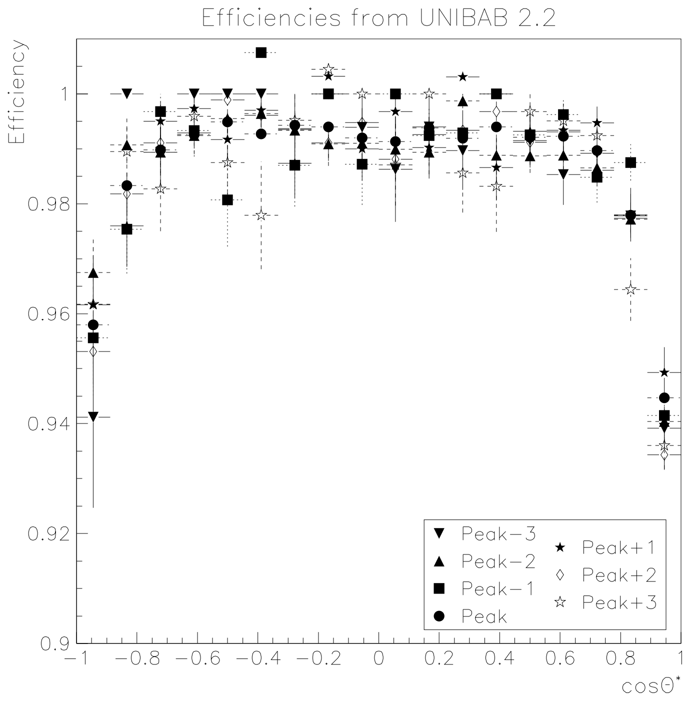

Figure 13: Signal Efficiency as a function of centre-of-mass.

To determine the contamination from background events a number of Monte Carlo datasets were analysed with the standard selection code. The number of events left from some of the various background data samples considered, as a function of the cut applied, is recorded in Table 15.

Cut / Channel Analysed	$\gamma\gamma$	$\tau^+\tau^-$	$q\overline{q}$	$\mu^+\mu^-$
Events Analysed	150000	1057000	4221358	281000
All track cuts	4.21400 ± 0.05187	87.71523 ± 0.03193	0.34436 ± 0.00285	91.68256 ± 0.05209
ΣE, Σp, ξ cuts	0.91800 ± 0.02462	77.51524 ± 0.04061	0.14837 ± 0.00187	90.84946 ± 0.05439
ΣE+Σp cut	0.00933 ± 0.00249	1.04816 ± 0.00991	0.00076 ± 0.00013	0.03772 ± 0.00366
$\cos\theta^*$ cut	0.00333 ± 0.00149	0.86471 ± 0.00901	0.00038 ± 0.00009	0.02847 ± 0.00318
Muon veto	0.00333 ± 0.00149	0.81675 ± 0.00875	0.00038 ± 0.00009	0.00107 ± 0.00062

Table 15: Summary of selection efficiency (in percent) as a function of the applied cut for background Monte Carlo samples analysed.

These results show that there is negligible background contamination from the channels $q\overline{q}$ ($< 7.10^{-5}$), $\gamma\gamma$ ($< 4.10^{-5}$) and $\mu\mu$ ($< 1.10^{-5}$). The only channel that contributes at a non-negligible level is from the irreducible source of background $\tau\tau$ where both taus decay into an electron and two neutrinos. This background contributes at the level of around 1.2%

of the total signal and varies as a function of $\cos\theta^*$ according to Figure 14. The level of background from the $\tau\tau$ channel is consistent within errors across the different Monte Carlo samples considered.

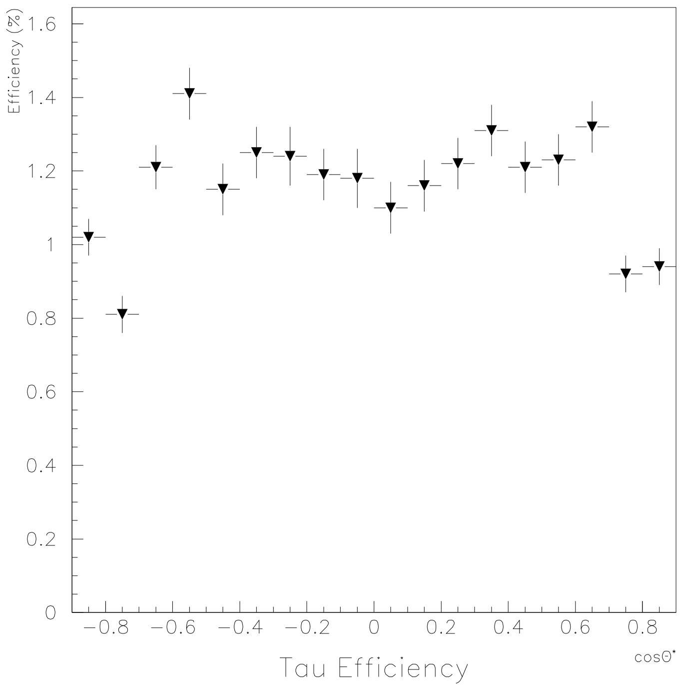

Figure 14: $\tau\tau$ efficiency as a function of $\cos\theta^*$.

9.4 Inclusive lepton selection

10 Measurement of lepton forward-backward asymmetry

10.1 Muon forward-backward asymmetry

10.2 Tau forward-backward asymmetry

10.3 Electron forward-backward asymmetry

11 Determination of Z resonance parameters

The parametrisation of the dominant contribution to the cross section at energies around the Z^0 resonance is based on a Breit-Wigner shape with an s-dependent width. After deconvolution of pure QED corrections, this is given in the "improved Born approximation" by

$$\sigma_{\mathrm{f\bar{f}}}(s) = \sigma^{0}_{\mathrm{f\bar{f}}} \frac{s\Gamma_{\mathrm{Z}}^{2}}{\left(s - M_{\mathrm{Z}}^{2}\right)^{2} + s^{2}\Gamma_{\mathrm{Z}}^{2}/M_{\mathrm{Z}}^{2}} \,, \tag{8}$$

where the parameters are the Z^0 mass, M_{Z} , the width, Γ_{Z}, and the pole cross section, $\sigma^0_{\mathrm{f\bar{f}}}$. The contributions from γ exchange and from γ–Z^0 interference are small at energies $\sqrt{s} = M_{\mathrm{Z}}/c^2$ and were set to their Standard Model values.

The pole cross section can be written in terms of partial decay widths of the initial and final states, Γ_{ee} and $\Gamma_{\mathrm{f\bar{f}}}$,

$$\sigma^{0}_{\mathrm{f\bar{f}}} = \frac{12\pi}{M_{\mathrm{Z}}^{2}} \frac{\Gamma_{\mathrm{ee}}\Gamma_{\mathrm{f\bar{f}}}}{\Gamma_{\mathrm{Z}}^{2}} \,. \tag{9}$$

The definition of the widths explicitly includes QED and QCD corrections,

$$\Gamma_{\mathrm{f\bar{f}}} = \frac{G_{\mathrm{F}} M_{\mathrm{Z}}^{3}}{6\pi\sqrt{2}} N_{c}^{\mathrm{f}} (g_{V_{\mathrm{f}}}^{2} + g_{A_{\mathrm{f}}}^{2})(1 + \delta_{QED} + \delta_{QCD}) \;; \tag{10}$$

$g_{V_{\mathrm{f}}}$ and $g_{A_{\mathrm{f}}}$ are effective vector and axial vector couplings of the Z^0 to fermion species f, and N_c^{f}, the QCD colour factor, is one for leptonic final states and three for hadrons. Due to the effect of radiative corrections, this effective couplings are complex numbers. Hereafter $g_{V_{\mathrm{f}}}$ and $g_{A_{\mathrm{f}}}$ refer to the real parts of the effective couplings, while the small imaginary components are fixed to the MSM predictions in the fitting procedure [19].

+ Z. Phys. C65 (1995) 267-276

The pole cross sections, $\sigma^0_{\mathrm{f\bar{f}}}$, have in common the statistical and systematic error from the luminosity determination. It is therefore more practical to use the ratios of pole cross sections in the parametrisation of the leptonic channels,

$$R_{\mathrm{f}} = \frac{\sigma^{o}_{\mathrm{had}}}{\sigma^{0}_{\mathrm{f\bar{f}}}} \equiv \frac{\Gamma_{\mathrm{had}}}{\Gamma_{\mathrm{f\bar{f}}}} \quad \text{for} \quad \mathrm{f\bar{f}} = \mathrm{e^+e^-}, \mu^+\mu^-, \tau^+\tau^- . \tag{11}$$

The errors on R_{e}, R_μ and R_τ are entirely dominated by the total error on the lepton cross sections, with very small correlations of about 5% from the common normalisation to the number of hadrons.

The energy dependence of the leptonic forward-backward asymmetry depends on the axial coupling which is mainly determined by the leptonic width. Therefore, the measurements of the leptonic forward-backward asymmetries can be condensed into one single parameter per lepton species in the final state, the pole asymmetry $\mathrm{A}^{0,\mathrm{f}}_{\mathrm{FB}}$. This is given by the following combinations of effective couplings

$$\mathrm{A}^{0,\mathrm{f}}_{\mathrm{FB}} \equiv \frac{3}{4} \mathcal{A}_{\mathrm{e}} \mathcal{A}_{\mathrm{f}} \tag{12}$$

with:

$$\mathcal{A}_{\mathrm{f}} \equiv \frac{2 g_{V_{\mathrm{f}}} g_{A_{\mathrm{f}}}}{g_{V_{\mathrm{f}}}^{2} + g_{A_{\mathrm{f}}}^{2}} \,. \tag{13}$$

The contributions from γ–Z^0 interference, imaginary parts of the photon vacuum polarisation, and the imaginary parts of the effective couplings are set to their Standard Model expectations and not included in the definition of $A_{FB}^{0,f}$.

11.1 The fit procedure

The nine parameters M_Z, Γ_Z, σ^o_{had}, R_e, R_μ, R_τ, $A_{FB}^{0,e}$, $A_{FB}^{0,\mu}$ $A_{FB}^{0,\tau}$ were fitted to the whole set of cross sections and forward-backward lepton asymmetries accumulated by ALEPH during the LEP-I period. This was done with the latest version of the computer code MIZA [19] and cross-checked with ZFITTER [20, 21]. These codes provide parametrisations of the fermion pair production cross sections and forward-backward asymmetries at energies around the Z^0 resonance in terms of effective couplings and also calculate pure QED corrections to full $\mathcal{O}(\alpha^2)$ with exponentiation.

The measured cross sections and forward-backward asymmetries were treated in a χ^2 minimisation procedure to extract the nine parameters and their errors and correlations. The full covariance matrix of the input measurements, $(\mathcal{V})$, was constructed to describe the correlations between statistical and systematic errors of the measurements. These comprise the statistical and systematic errors of the luminosity measurements entering into all cross section determinations, the detector acceptance and efficiencies, the LEP beam energy uncertainties common to all channels, and uncertainties in the theoretical calculations, which are dominated by the uncertainty on the small angle bhabha cross section and the t-channel contribution to the wide angle bhabhas.

χ^2 is given in terms of the vector of measurements, $\left(\sigma^j, A^j_{FB}\right)$, the vector of theoretical predictions, $\left(\sigma^t(f\bar{f}, E_i, \mathbf{p}), A^t_{FB}(f\bar{f}, E_i, \mathbf{p})\right)$, depending on the parameter vector $\mathbf{p} = (M_Z, ..., A_{FB}^{0,\tau})$, and the covariance matrix, $(\mathcal{V})$, of the measurements by

$$\begin{array}{rcl} \chi^2 & = & \Delta^T \cdot (\mathcal{V})^{-1} \cdot \Delta \ \ \text{with} \\ \Delta & = & \left(\sigma^t(f\bar{f}, E_i, \mathbf{p}), A^t_{FB}(f\bar{f}, E_i, \mathbf{p})\right) - \left(\sigma^j, A^j_{FB}\right) \end{array} \tag{14}$$

The dependence of the theoretical predictions for the cross sections and asymmetries on the parameters $\mathbf{p}$ are calculated for each final state, $f\bar{f}$, and each energy, E_i. The measured values of the nine parameters of interest, denoted by the vector $\mathbf{p}$, are determined by the set of numbers for which χ^2 becomes minimal. The minimisation procedure also determines the correlation coefficients between the parameters.

11.1.1 Treatment of energy errors

The covariance matrix elements of the energy determination, $(\mathcal{V}^E)_{i,j}$ are propagated into errors on the measured cross sections via

$$(\mathcal{V})^{energy}_{i,j} = \frac{d\sigma(E_i)}{dE} \cdot (\mathcal{V}^E)_{i,j} \cdot \frac{d\sigma(E_j)}{dE} \ .$$

The spread of the centre-of-mass energy due to the natural spread in energy of the beam particles leads to a correction given by

$$\delta\sigma(E) \approx -\frac{1}{2}\frac{d^2\sigma(E)}{dE^2}\delta E^2 \ .$$

This correction induces a change in the cross section at $\sqrt{s} = M_{\mathrm{Z}}$ of 0.16%, which feeds through to a decrease of Γ_{Z} of about 5 MeV. The effect on M_{Z} and other parameters is negligible.

11.2 Fit results

The results of the nine-parameter fit are shown in table 16. The χ^2 per degree of freedom is 173/176, corresponding to a χ^2-probability of 55 %.

The values obtained for R_ℓ and $\mathrm{A}_{\mathrm{FB}}^{0,\ell}$ for the different lepton species are identical within errors, in agreement with the assumption of universality of the Z^0 couplings to leptons. Note that mass corrections lead to a value of R_τ which is expected to be about 0.2% smaller than for the light leptons.

The fits were repeated reducing the number of parameters from nine to five assuming universal quantities R_ℓ and $\mathrm{A}_{\mathrm{FB}}^{0,\ell}$. Here, the leptonic width is defined as the partial Z^0 decay width into a pair of massless leptons. The results are also shown in table 16. These five measurements constitute the minimal and at the same time most precise set of parameters needed to describe the dependence on Z^0 parameters of the differential cross section near the Z^0 resonance.

Figures 15 and 16 show the data points and a solid line representing the fit results. Good agreement ... .
plots to be worked on !!

The contour lines of the ratios of hadronic and leptonic widths and of the pole asymmetries from the nine and five parameter fits are shown in figure 11.2.

11.3 External errors

Table 16 gives the full error on our measurements. However, not all are really experimental due to external sources of uncertainties. These are quantified in the following subsections.

11.3.1 Luminosity errors

The error of 0.11 % on the theoretical bhabha cross section [?] directly feeds through into an uncertainty on the hadronic pole cross section of 0.46 nb. Other parameters are not affected by this.

		correlation matrix								
		M_Z	Γ_Z	σ^o_{had}	R_e	R_μ	R_τ	$A^{0,e}_{FB}$	$A^{0,\mu}_{FB}$	$A^{0,\tau}_{FB}$
M_Z [GeV]	91.1883±0.0031	1.00	0.05	−0.01	0.00	−0.03	−0.02	0.02	0.05	0.04
Γ_Z [GeV]	2.4951±0.0043		1.00	−0.16	−0.00	−0.01	−0.00	−0.00	−0.00	0.00
σ^o_{had} [nb]	41.520 ±0.068			1.00	0.06	0.11	0.08	0.00	0.00	0.00
R_e	20.659±0.088				1.00	0.05	0.04	−0.02	0.01	0.00
R_μ	20.820±0.061					1.00	0.06	−0.00	0.01	−0.00
R_τ	20.769±0.071						1.00	−0.00	0.00	0.01
$A^{0,e}_{FB}$	0.0176±0.0037							1.00	0.01	0.01
$A^{0,\mu}_{FB}$	0.0170±0.0025								1.00	0.02
$A^{0,\tau}_{FB}$	0.0167±0.0028									1.00

		correlation matrix				
		M_Z	Γ_Z	σ^o_{had}	R_ℓ	$A^{0,\ell}_{FB}$
M_Z [GeV]	91.1883±0.0031	1.00	0.04	−0.02	−0.02	0.06
Γ_Z [GeV]	2.4951±0.0043		1.00	−0.15	0.00	0.00
σ^o_{had} [nb]	41.520 ±0.068			1.00	0.14	0.00
R_ℓ	20.754±0.043				1.00	0.01
$A^{0,\ell}_{FB}$	0.0170±0.0017					1.00

Table 16: Results of the five and nine parameter fits to the cross section and asymmetry data. Shown are the total errors and the full correlation matrix of the measurements.
numbers to be replaced by final fit!

11.3.2 Errors from LEP beam energy uncertainty

The contribution of energy related uncertainties to the error on the nine parameters were determined by reducing the experimental errors to half their original value, whereas the energy related uncertainties were left unchanged. Although it is not strictly possible to write the squared total error as a quadratic sum of two components, a good approximation of this error is obtained that way, which is in agreement with the naive expectations (see equation 1). The error matrix of the energy contribution, (C_E) is determined by

$$(C_E) = \frac{4}{3}(\mathcal{C}_{1/2}) - \frac{1}{3}(\mathcal{C}) \ , \qquad (15)$$

where $(\mathcal{V}_{1/2})$ is the covariance matrix of the fitted parameters with halved experimental errors, and $(\mathcal{C})$ is the original error matrix of the 9 parameters as introduced above. The most significant contributions from energy-related errors are shown in table 17. Compared with other errors, only the contribution to the errors on M_Z and Γ_Z is important, which amounts to 1.5 MeV and 1.2 MeV, respectively. The anti-correlation between the electron asymmetries and the μ and τ asymmetries is due to the negative slope in the energy dependence of the electron asymmetry from the t-channel contribution.

The uncertainties on the energy spread, given in the caption of table 2, lead to an uncertainty of 0.3 MeV on Γ_Z, to a negligible contribution of 0.005 nb to the error on σ^o_{had}, and are totally negligible for other parameters.

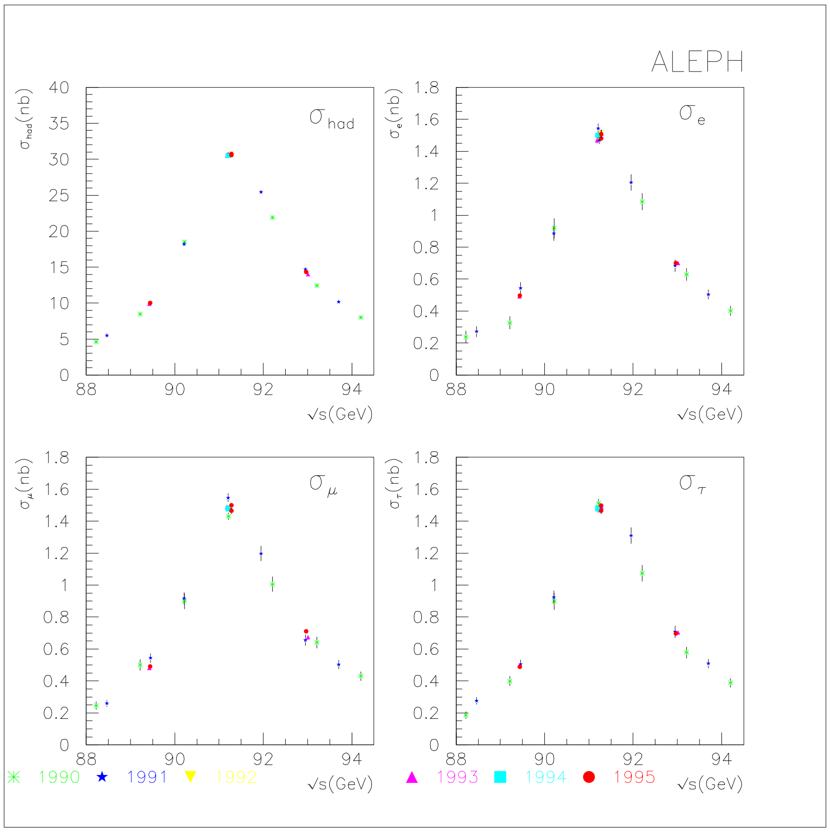

Figure 15: Measurements of cross sections.

(C_E)	M_Z [MeV]	Γ_Z [MeV]	$\sigma^o_{\rm had}$ [nb]
M_Z [MeV]	1.5^2	-0.4^2	-0.08^2
Γ_Z [MeV]		1.2^2	-0.08^2
$\sigma^o_{\rm had}$ [nb]			0.0095^2

	$A_{FB}^{0,e}$	$A_{FB}^{0,\mu}$	$A_{FB}^{0,\tau}$
$A_{FB}^{0,e}$	0.00027^2	-0.00018^2	-0.00018^2
$A_{FB}^{0,\mu}$		0.00023^2	0.00023^2
$A_{FB}^{0,\tau}$			0.00023^2

Table 17: *The contribution of LEP energy uncertainties to the errors on parameters derived from line shape and asymmetry measurements, given as covariance matrix elements.*

11.3.3 Uncertainty from t-channel

to be worked on

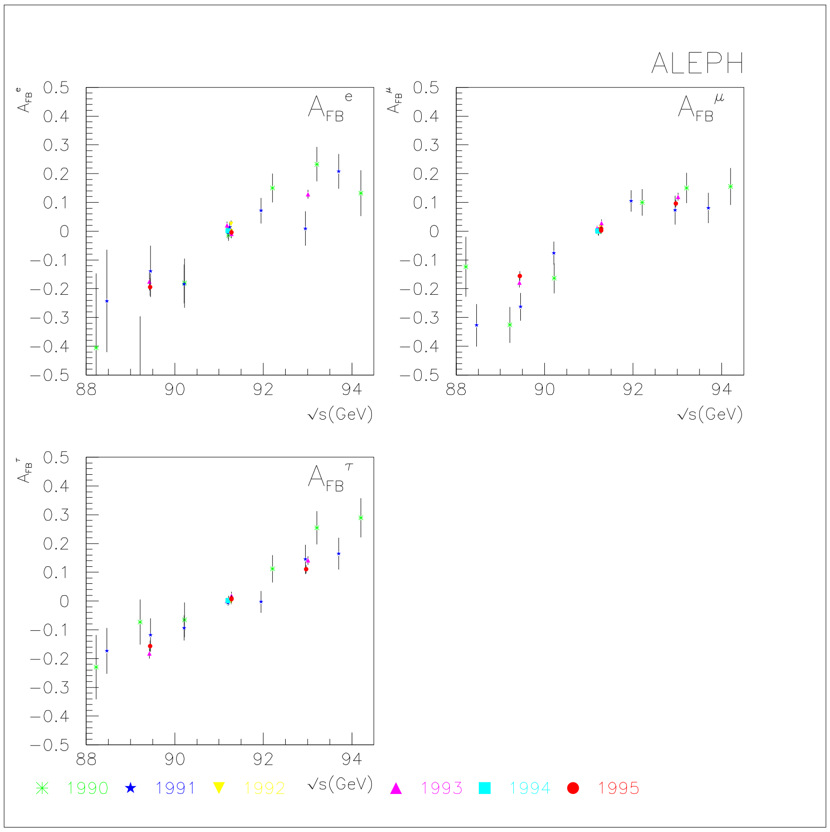

Figure 16: Measurements of forward-backward asymmetries.

11.3.4 Residual Standard Model dependence

Some terms in the fits were fixed to their Standard Model values, and this may influence the results. By varying the input parameters, these effects can be quantified within the Standard Model. Effects significant compared to the experimental errors were only seen for M_Z. Variations of the Higgs boson mass between 70 GeV and 1000 GeV dominates, whereas Other parameter variations within their present errors have much smaller effects, leading to a total error of ± 0.3 MeV on M_Z due to Standard Model uncertainties. This is negligible if added in quadrature to the experimental errors.

11.3.5 Uncertainty from radiative corrections

A comparison of fit results obtained with MIZA or with ZFITTER showed as the only significant difference a deviation in $\sigma^o_{\rm had}$ of 0.01 nb. The estimated precision of the radiative corrections is 0.1 % [**?**], leading to a similar uncertainty on the pole cross sections. These uncertainties are small compared to the theoretical error in the luminosity determination. **probably more needed here**

Figure 17: The ratio of leptonic and hadronic widths vs. the pole asymmetry for all lepton species separately and assuming lepton universality. The shaded area shows the Standard Model expectation.

11.4 Interpretation of results

11.4.1 Partial Z^0 decay widths

By parameter transformation from the original nine and five parameters we can obtain the partial decay widths into hadrons and leptons, shown in table 18.

Since the total Z^0 width is the sum of all partial widths, the decay width into invisible particles, $\Gamma_{\rm inv}$, can also be determined:

$$\Gamma_{\rm inv} = \sqrt{\frac{12\pi R_{\rm l}}{M_{\rm Z}^2 \sigma^o_{\rm had}}} - \Gamma_{\rm had} - 3\,\Gamma_{\ell\ell}\,(1+\delta_m)\ , \qquad (16)$$

where $\delta_m = -0.0023$ is a small correction which accounts for the tau mass effect.

The results are summarised in table 18. The comparison of the partial decay widths of the Z^0 into e, μ and τ shows good consistency with lepton universality.

To check whether the invisible width is completely explained by decays into the three

	without	with
	lepton universality	
Γ_{had} [MeV]	1739.2±4.8	1743.2±3.6
Γ_{inv} [MeV]	503.5±3.9	500.1±2.7
$\Gamma_{\text{inv}}/\Gamma_{\ell\ell}$	-	5.954±0.029
$\Gamma_{\ell\ell}$ [MeV]	-	83.99±0.15
Γ_{ee} [MeV]	84.19 ±0.22	-
$\Gamma_{\mu\mu}$ [MeV]	83.54 ±0.32	-
$\Gamma_{\tau\tau}$ [MeV]	83.74 ±0.35	-

Table 18: Partial Z^0 decay widths, obtained by parameter transformation from the nine and five parameter fits of table 16.

neutrino species, the "number of neutrinos", N_ν can be calculated according to

$$\frac{\Gamma_{inv}}{\Gamma_l} = N_\nu \cdot \left(\frac{\Gamma_\nu}{\Gamma_l}\right)_{SM} \quad . \tag{17}$$

The Standard Model value for the ratio of the partial widths to neutrinos and to charged leptons has a very small error, since the top and Higgs mass dependences and very small QCD corrections largely cancel.

$$\left(\frac{\Gamma_\nu}{\Gamma_l}\right)_{SM} = 1.991 \pm 0.001 \; ; \tag{18}$$

where the uncertainty arises from variations of the top quark mass within $M_{\text{t}} = 175.6 \pm 5.5$ GeV and of the Higgs mass within 70 GeV $< \text{M}_{\text{H}} <$ 1000 GeV.

With our measured value of $\Gamma_{inv}/\Gamma_l = 5.954 \pm 0.029$ N_ν becomes 2.990 ± 0.015

If $N_\nu = 3$ is assumed, the measurement of N_ν can be turned into a measurement of Γ_ν/Γ_l:

$$\frac{\Gamma_\nu}{\Gamma_l} = 1.9846 \pm 0.0098$$

in good agreement with the Standard Model prediction given above. With $\Gamma^{\text{SM}}_{\nu\nu} = 167.12 \pm 0.2$ MeV the limit on any non-Standard Model contribution to the invisible width is

$$\begin{aligned} \Gamma^{\text{x}}_{\text{inv}} &= \Gamma_{\text{inv}} - 3\Gamma^{\text{SM}}_{\nu\nu} \\ &= -1.3 \pm 2.7\; MeV \\ &< 5.2 \text{ MeV at } 95\,\% \text{ C.L.}\,, \end{aligned}$$

where, conservatively, $\Gamma^{\text{x}}_{\text{inv}}$ was allowed to take only positive values when deriving the limit.

11.5 Z^0 couplings to leptons

More insight into the validity of lepton universality can be obtained by disentangling the initial and final state couplings by performing a fit for individual effective couplings, $g_{V_{\text{e}}}$, g_{V_μ},

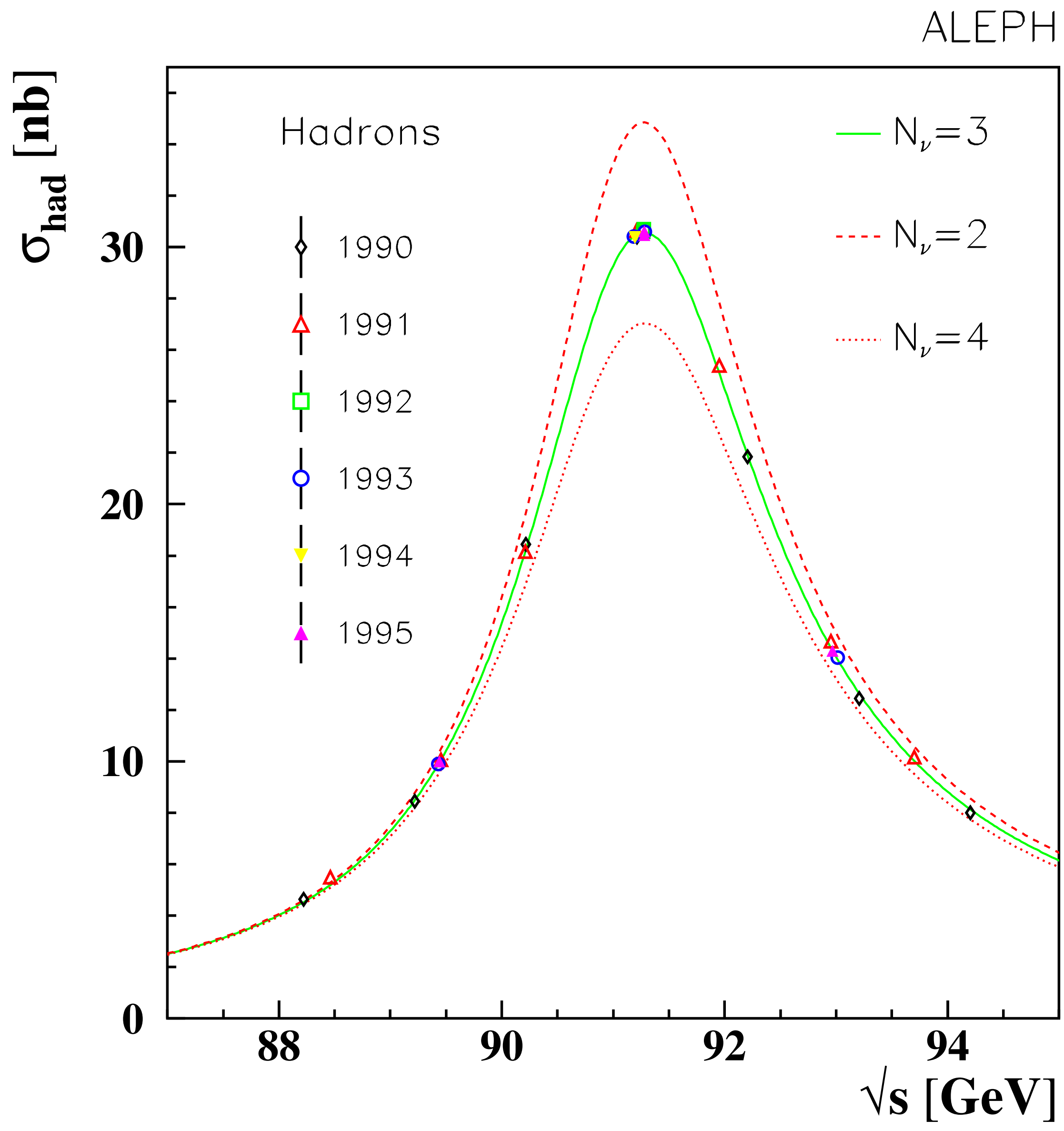

Figure 18: The hadron lineshape measured at ALEPH versus the expectation for $N_\nu = 2$, 3 and 4.

g_{V_τ}, g_{A_e}, g_{A_μ} and g_{A_τ}. Since our measured observables depend on the squares of couplings or on the ratio of g_{V_f}/g_{A_f}, there is a remaining ambiguity in all signs. The results are summarised in table 11.5.

Do we also want an analysis of couplings from LS alone and from Asym. alone? By performing such fits to the full cross section and asymmetry data, the energy dependence fixes the relative signs of electron and mu or tau couplings; only the sign of gv/ga remains ambiguous! Such a fit also quantifies the importance of the

$\lvert g_{V_e} \rvert$	0.0387 ± 0.0041
$\lvert g_{V_\mu} \rvert$	0.0372 ± 0.0066
$\lvert g_{V_\tau} \rvert$	0.0366 ± 0.0073
$\lvert g_{A_e} \rvert$	0.50178 ± 0.00073
$\lvert g_{A_\mu} \rvert$	0.4999 ± 0.0011
$\lvert g_{A_\tau} \rvert$	0.5012 ± 0.0012
$\lvert g_{V_\ell} \rvert$	0.0380 ± 0.0019
$\lvert g_{A_\ell} \rvert$	0.50125 ± 0.00048

Table 19: Results for the leptonic effective vector and axial vector couplings without and with the assumption of lepton universality.

assumption of SM slopes of the asymmetries without going through the pain of a full S-Matrix analysis. (do we want such a fit?)

The effective ρ parameter is entirely dominated by our measurement of the leptonic partial width with a small contribution from the invisible width. From our line shape measurements we obtain $\Delta\rho_{\mathrm{eff}}^{\mathrm{lept}} = 0.0052 \pm 0.0019$. The hadronic decay width only contributes if an external measurement of the strong coupling constant is used and if assumptions on flavour-dependent vertex corrections to the quark couplings are made. However, this would only result in a reduction of the error on $\Delta\rho_{\mathrm{eff}}^{\mathrm{lept}}$ by $\sim$5 %.

The pole asymmetries depend on the ratio of effective vector and axial vector couplings and hence the effective Weinberg angle, $\sin^2\theta_{eff}^{\mathrm{lept}}$, defined via the relation

$$g_{V_\ell}/g_{A_\ell} = (1 - 4\sin^2\theta_{eff}^{\mathrm{lept}}) \; . \tag{19}$$

From the measured lepton forward-backward asymmetry we obtain $\sin^2\theta_{eff}^{\mathrm{lept}} = 0.23106 \pm 0.00094$. Here the sign of g_{V_ℓ}/g_{A_ℓ} was chosen to be positive, in agreement with results from τ polarisation measurements.

The ratio of the hadronic and leptonic widths, R_ℓ, depends only very little on m_t and M_H due to cancellations, whereas it has a large dependence on the strong coupling constant, given to first order in α_s by

$$R_\ell \sim R_\ell^0(1 + \alpha_s(M_Z)/\pi) \; . \tag{20}$$

Therefore it allows a direct determination of $\alpha_s(M_Z)$ with minimum theoretical uncertainties. Using the full calculation with QCD predictions known to $\mathcal{O}(\alpha_s^3)$, one gets

$$\alpha_s(M_Z^2) \quad = \quad 0.1199 \pm 0.0064 \pm 0.002_{ew} \pm 0.002_{QCD} \pm 0.002_{M_H}$$

where the second and third error reflect uncertainties on the electroweak and QCD parts of the theoretical prediction, respectively [22], and the last one comes from the unknown Higgs mass.

A full Standard Model fit with α_s and M_{H} as free parameters and M_{t} [**?**] and $\alpha(M_{\mathrm{Z}})$ [**?**] constrained to their measured value also uses the information on α_s in the hadronic pole cross section. Here we obtain

$$\alpha_s(M_Z^2) \quad = \quad 0.1151^{+0.0055}_{-0.0051} \pm 0.002_{QCD} \ .$$

should we do more with SM fits to 5 and 9 parameters?

11.6 τ polarisation measurements and lepton universality

only can put this chapter if τ results published!

Figure 19: The 68% probability contours in the $g_{V_l} - g_{A_l}$ plane coming from the ALEPH leptonic measurements compared to the MSM predictions.

A deeper test on lepton universality can be carried out by analysing simultaneously the information coming from the lepton partial widths and the leptonic forward-backward and tau polarisation asymmetries. From these measurements the vector and axial couplings of the Z to each lepton species can be directly disentangled. The ALEPH results (see table **??** and fig. 19) show perfect agreement with the hypothesis of lepton universality for both, the vector and axial couplings.

$$g_{A_\mu}/g_{A_e} = 1.0014 \pm 0.0021 \ , \ g_{A_\tau}/g_{A_e} = 1.0034 \pm 0.0023 \ ,$$

$$g_{V_\mu}/g_{V_e} = 0.83 \pm 0.16 \qquad , \ g_{V_\tau}/g_{V_e} = 1.044 \pm 0.091 \ .$$

Figure 20: The ALEPH averages for $\sin^2\theta^{lept}_{eff}$ obtained from the different asymmetry observables discussed in the text.

12 Standard Model interpretation

only can put this chapter if enough interesting results published!

The results presented in the previous sections can be interpreted in the context of the Minimal Standard Model allowing a check of its validity in describing all the observations, and enabling the inference of some of the MSM unknown (or badly known) parameters.

The comparison is made through a fit of the measurements shown in table **??** to their MSM predictions in terms of the top quark mass m_t, the value of $\alpha_s(M_Z)$ and the Higgs mass. Since the sensitivity to the Higgs mass is small, the Higgs boson mass is, either fixed to 300 GeV and, afterwards, varied in the range between 70 and 1000 GeV when the external constraints on the top mass and $\alpha_s(M_Z^2)$ are not used, or left free when these quantities are constrained by their direct measurements.

The most up-to-date MSM calculations have been used [24, 20] and their estimated theoretical uncertainties have been also propagated in the fitting procedure, being the uncertainty $\Delta\alpha^{-1}) = 0.09$, due to the contribution of light quarks in the photon vacuum-polarisation, the one that dominates by far [21].

The results of the fit can be gleaned from table **??**. As can be seen in that table, the quality of all fits is good, and therefore we can claim that the MSM is able to describe well all the measurements discussed at their present (high) precision level. Moreover the m_t and $\alpha_s(M_Z^2)$ values resulting from these fits are in excellent agreement with the top mass determination at TEVATRON experiments of $m_t = 175.5 \pm 5.5$ GeV and with the world average determination of the strong coupling constant of $\alpha_s(M_Z^2) = 0.118 \pm 0.003$. Hence, there is evidence that the bulk of non-trivial quantum effects in precision electroweak observables is indeed due to the top quark as predicted by the MSM.

The Higgs mass that the precision ALEPH data prefers is in good agreement with the expected range within the MSM although its uncertainty does not allow a detailed scrutinization of the Higgs sector.

A Trigger efficiency

$q\overline{q}$	efficiency(%)
1990 data	?? ± ??
1991 data	100.00 ± 0.0038
1992 data	100.00 ± 0.003
1993 data	100.00 ± 0.009
1994 data	100.00 ± 0.005
1995 data	?? ± ??
tot data	?? ± ??

Table 20: Trigger efficiencies for hadronic events.

$\tau^+\tau^-$	efficiency(%)
Monte Carlo	99.99752±0.00025
1990 data	99.99664±0.00079
1991 data	99.99705±0.00053
1992 data	99.99614±0.00042
1993 data	99.99585±0.00044
1994 data	99.99680±0.00025
1995 data	99.99643±0.00039
tot data	99.99648±0.00016

Table 21: Trigger efficiencies for tau events obtained from data and Monte Carlo.

Year	Electromagnetic track trigger	Total energy trigger
MC	0.99995 ± 0.00001	$1.00000^{+0.00000}_{-0.00001}$
1990	0.99990 ± 0.00010	$1.00000^{+0.00000}_{-0.00019}$
1991	0.99968 ± 0.00013	$1.00000^{+0.00000}_{-0.00010}$
1992	0.99993 ± 0.00004	$1.00000^{+0.00000}_{-0.00005}$
1993	0.99988 ± 0.00005	$1.00000^{+0.00000}_{-0.00004}$
1994	0.99993 ± 0.00003	0.99994 ± 0.00001
1995	0.99994 ± 0.00004	$1.00000^{+0.00000}_{-0.00004}$

Table 22: Summary of Bhabha trigger efficiencies

B Monte Carlo sets

Run	$\sqrt{s}$ (GeV)	Geom.	Galeph	Julia	# events
1757	91.200	1993^{I}	256.02	276.04	100K
944	91.200	1994^{IV}	303	278.01	90K
1830	91.200	1994^{IV}	304.10	282	100K
1840	91.200	1994^{IV}	304.10	282	100K
1850	91.200	1994^{IV}	304.10	282	100K
1860	91.200	1994^{IV}	304.10	282	100K
1870	90.210	1994^{IV}	304.11	282	50K
1880	92.070	1994^{IV}	304.11	282	50K
1810	93.000	1993^{II}	303	278.02	50K
1820	89.500	1993^{II}	303	278.02	50K
1890	88.360	1994^{IV}	304.11	282	50K
1900	93.920	1994^{IV}	304.11	282	50K

Table 23: Summary of $\mu^+\mu^-$ (KORALZ) Monte Carlo samples used in the analysis.

Run	$\sqrt{s}$ (GeV)	Geom.	Galeph	Julia	# events
1734	91.250	1993^{III}	256.02	276.04	100K
1735	91.250	1993^{III}	256.02	276.04	100K
1736	91.250	1993^{III}	256.02	276.04	100K
440	91.250	1994^{I}	303	278.02	100K
914	91.250	1994^{IV}	303	278.01	90K
924	91.250	1994^{IV}	303	278.01	87K
934	91.250	1994^{IV}	303	278.01	90K
1744	91.250	1994^{IV}	303	278.01	100K
1474	91.250	1994^{IV}	303	278.01	90K
1750	93.014	1993^{I}	256.02	276.04	97.5K
1753	93.014	1993^{I}	256.02	276.04	100K
1754	89.432	1993^{I}	256.02	276.04	100K

Table 24: Summary of $\tau^+\tau^-$ (KORALZ) Monte Carlo samples used in the analysis.

Year (Geometry)	Energy (GeV)	Events Generated	Cross-Section (nb)	Equivalent Luminosity (pb^{-1})
1992	88.344	10000	1.0618	9.42
1994	89.438	30000	1.3380	22.42
1992	90.215	10000	1.6911	5.91
1994	91.187	356976	1.9392	184.08
1992	92.207	10000	1.2852	7.78
1994	92.970	30000	0.9347	32.10
1992	93.952	10000	0.7150	13.99
1993	91.250	89982		

Table 25: Summary of e^+e^- (UNIBAB) Monte Carlo samples used in the analysis.

References

[1] ALEPH Collaboration, Nucl. Instr. Methods **A294** (1990) 121.

[2] ALEPH Collaboration, Nucl. Instr. Methods **A360** (1995) 481.

[3] G. Batignani *et al.*, 1991 IEEE Nuclear Science Symposium, Santa Fe, IEEE Transactions on nuclear science, NS 39(4-5) (1992) Vol.1, 438.

[4] G.J. Barber *et al.*, Nucl. Instr. Methods **A279** (1989) 212.

[5] W.B. Atwood *et al.*, Nucl. Instr. Methods **A306** (1991) 446.

[6] L. Arnaudon *et al.*, *The Energy Calibration of LEP in 1991*, CERN-PPE/92-125 (1992) and CERN-SL/92-37(DI);
LEP Energy Working Group, ALEPH, DELPHI, L3 and OPAL Collaborations, L. Arnaudon *et al.*, Phys. Lett. **B307** (1993) 187;
LEP Energy Working Group, L. Arnaudon *et al.*, *The Energy Calibration of LEP in 1992*, CERN SL/93-21 (DI), April 1993;
LEP Energy Working Group, L. Arnaudon *et al.*, *Accurate determination of the LEP beam Energy by resonant depolarization*, CERN-SL/94-71 (BI), August 1994.

[7] L.Arnaudon *et al.*, Phys. Lett. **B284** (1992) 431.

[8] S. Jadach, B.F.L. Ward, Z. Wąs, Comp. Phys. Comm. **66** (1991) 276, **79** (1994) 503;
S. Jadach, Z. Wąs, R. Decker, M. Ježabek, J.H. Kühn, Comp. Phys. Comm. **76** (1993) 361.

[9] H. Anlauf, P. Manakos, T. Ohl, T. Mannel, H. Meinhard, H.D. Dahmen, Comp. Phys. Comm. **79** (1994) 466.

[10] J.E. Campagne and R. Zitoun, Z.Phys. **C43** (1989) 469.

[11] T. Sjostrand, Comp. Phys. Comm. **82** (1994) 74.

[12] ALEPH Collaboration,
detector
Z.Phys. **C53** (1992) 375.

[13] A.Bazarko et al., "Final luminosity and systematic errors for the 1994 Electroweak selection", ALEPH Note 96-020 (PHYS 96-019).

[14] S. Jadach et al., CERN-TH /95-38 and *Phys. Lett.* **B353** (1995) 362.
S. Jadach et al., *Phys. Lett.* **B353** (1995) 349.

[15] S. Jadach et al., BHLUMI 4.04, CERN-TH /96-158 and UTHEP-96-0601 (submitted to *Comp. Phys. Comm.*).
S. Jadach et O.Nicrosini, "Event generators for Bhabha scattering ", in "Physics at LEP2 ", CERN 96-01 Vol.2, February 1996.

[16] W. Beenakker and B. Pietrzyk, *Phys. Lett.* **B296** (1992) 241,*Phys. Lett.* **B304** (1993) 366.

[17] ALEPH Collaboration,
Z.Phys. **C62** (1994) 539.

[18] see *e.g.* F.A. Berends *et al.* , *Proceedings of the Workshop on Z physics at LEP I*, CERN Report 89-08 Vol.I, 89.

[19] M Martinez, L. Garrido, R. Miquel, J.L. Harton and R. Tanaka, Z.Phys. **C49** (1991) 323.

[20] D. Bardin *et al.*, Z. Phys. **C44** (1989) 493; Comp. Phys. Comm. **59** (1990) 303; Nucl. Phys. **B351**(1991) 1; Phys. Lett. **B255** (1991) 290 and CERN-TH 6443/92 (May 1992).

[21] *Reports of the working group on precision calculations for the Z resonance*, eds. D. Bardin, W. Hollik and G. Passarino, CERN Yellow Report 95-03, Geneva, 31 March 1995. and references therein.

[22] T. Hebbeker, M. Martinez, G. Passarino and G. Quast, Phys. Lett. **B331** (1994) 165, and references therein.

[23] S. Eidelmann and F. Jegerlehner, Z. Phys. **C67** (1995) 585;
H. Burkhardt and B. Pietrzyk, Phys. Lett. **B356** (1995) 398.

[24] G. Burgers, W. Hollik and M. Martinez; M. Consoli, W. Hollik and F. Jegerlehner: *Proceedings of the Workshop on Z physics at LEP I*, CERN Report 89-08 Vol.I, 7; G. Burgers, F. Jegerlehner, B. Kniehl and J. Kühn: the same proceedings, CERN Report 89-08 Vol.I, 55.